AUSTRIAN
MARSHALL PLAN FOUNDATION
VIENNA | AUSTRIA

MARSHALL PLAN SCHOLARSHIP RESEARCH REPORT

CRYOGENIC NANOINDENTATION OF SINGLE CRYSTALLINE COPPER, CHROMIUM AND TUNGSTEN

Raphael Esterl

Adviser

Assoc. Prof. Dr. Daniel Kiener

Montanuniversität Leoben, Austria

Co-Adviser

Assoc. Prof. Dr. Peter Hosemann

University of California, Berkeley, USA.

This work has been carried out at the Department of Materials Physics, Montanuniversität Leoben, Austria, in cooperation with the Department of Nuclear Engineering, University of California, Berkeley, USA.

September 1, 2015

Affidavit

I declare in lieu of oath that my thesis is the result of my own work. I did not receive any help of support from commercial consultants. All sources and / or materials applied are listed and specified in the thesis.

Eidesstattliche Erklärung

Hiermit erkläre ich an Eides statt, die Arbeit eigenständig verfasst und keine anderen als die von mir angegebenen Quellen und Hilfsmittel verwendet zu haben.

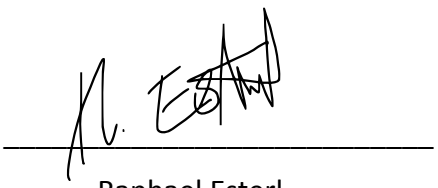

Leoben, September 1, 2015 Raphael Esterl

Acknowledgements

In the first place I want to thank my supervisor Assoc. Prof. Daniel Kiener for the opportunity to write the work at the Department of Materials Physics. I want to express my strongest gratitude for his encourages, support and advises throughout the whole work. I appreciate the friendly relation during my entire work at the Department.

Needless to say, I am highly obliged to Assoc. Prof. Peter Hosemann for the opportunity to use the facilities at the Department of Nuclear Engineering at UC Berkeley and his scientific advice. I want to thank his entire group and am especially grateful to David Frazer and AJ Gubser for their introduction and consistent assistance at the FIB facility.

I want to thank the whole Erich Schmid Institute in Leoben. Ahead of all, I'm very grateful to Dr. Verena Maier for the professional guidance and mentoring in all nanoindentation concerns. I want to thank Dr. Thomas Schöberl and Silke Modritsch for their technical assistance and sample preparation and Dipl.-Ing. Reinhard Fritz for his helpful advises. Moreover I want to give props to Dipl. Ing. Thomas Leitner for his assistance. Needless to say I want to thank my very good friends Dipl.-Ing. Alexander "Lexi" Leitner and Josef "Joe" Pörnbacher for their outraging support in technical queries and the inspiring and encouraging discussions. I am deeply grateful for their friendship including the whole "Muli-troop" which engraved the times of my entire studies.

Furthermore, I owe the Austrian Marshall Plan Foundation a debt of gratitude for their generous financial support without this work could not have been realized.

Finally I am indebted to my whole family, which played an important role in the success of my studies and especially to my father, Robert Esterl who has always been the major idol in my life for his encouraging support and financial assistance.

Abbreviations and symbols

A_c ..... Projected contact area

AFM ..... Atomic force microscope

bcc ..... Body centered cubic

C_f ..... Frame compliance

CT ..... Cryogenic temperature

E ..... Young's modulus

EBSD ..... Electron back scattered diffraction

E_i ..... Young's modulus of the indenter

E_r ..... Reduced modulus

ESI ..... Erich Schmid Institute

F ..... Load

fcc ..... Face centered cubic

FIB ..... Focused ion beam

GNDs ..... Geometrically necessary dislocations

H ..... Hardness

H_0 ..... Macroscopic hardness

h_c ..... Contact depth

HV ..... Vickers hardness

ISE ..... Indentation Size Effect

LC ..... Load controlled

RT ..... Room temperature

S ..... Stiffness

SEM ..... Scanning electron microscope

SSDs ..... Statistically stored dislocations

sx ..... Single crystal, single crystalline

T_c ..... Critical temperature

τ_{th} ..... Theoretical shear strength

Contents

1. Introduction

In times of increasing digitalization and decreasing size of structural components the knowledge of the mechanical properties of materials at small scales becomes inalienable. “There’s Plenty of Room at the Bottom” quoted Richard Feynman at the California Institute of Technology on December 29, 1959 and called his audience attention to the important interest in comprehending structural correlations of materials at very little dimensions [1]. Just years later the term “nanotechnology” was born and Binning, Quate and Gerber achieved first successes to image atomic scales introducing the atomic force microscope (AFM) in 1985 [2]. Nevertheless over 50 years after Feynman’s first introduction to small scales, there is still plenty of room at the bottom and the research on dimensional aspect must be extended through investigations on temperature dependent properties. The wide application spectrum of modern materials requires a fundamental comprehension on the behavior of materials at different temperatures. The influence of temperature on the material performance has been a matter of scientific interest for the last decades and is subject to numerous research investigations. Though by now, the main focus has been held on material behavior at elevated temperatures, due to the fact that material application at higher temperatures prevailed those at lower temperatures. The ductile-to-brittle transition temperature (DBTT) is the common expression to define the utilization of material regarding its temperature. Below the DBTT body centered cubic (bcc) materials deform brittle, they rather tend to fracture on impact than to deform plastically. This leads to a temperature dependent deformation behavior below a characteristic critical temperature due to the fact that the specific shear stress of the material, which is necessary for deformation, increases [3]. Since the deformation of metals is incumbent upon the mobility of dislocation, its kinetic follows to be delimitated at low temperatures. To investigate various material characteristics, nanoindentation has established itself successfully as distinctive technique to examine deformation behaviors [4]. In the context of nanomechanical hardness testing two peculiarities protrude, which are of major interest to be examined at lower temperatures. The main interest of the present thesis is the so-called Indentation Size Effect (ISE), which manifests itself in a dimensional related change of mechanical properties. Whereas the major focus of investigation will be on its temperature dependence below room temperature (RT).

Furthermore, the so-called “pop-in” event will be examined, which characterizes the transition from elastic to plastic deformation. Fleck et al. tried first to explain the ISE with large strain gradients inherent in small indentations leading to geometrically necessary dislocations that cause enhanced hardening [5,6]. Nix and Gao followed with their investigations on Cu single crystals to find a law for the strain gradient plasticity [7]. Towards that, the present thesis should contribute to their work with explorations at cryogenic temperatures. Additionally, the research on the cryogenic deformation of single crystalline Cr and W will provide the insight of the deformation mechanism of body centered cubic metals. I hope to contribute with my study concerning the cryogenic deformation mechanisms of both face- as well as body centered cubic materials to the existing body of knowledge.

2. Theoretical background

2.1. Mechanical properties of fcc and bcc metals

Metals exist in different crystalline structures. We mostly distinguish between a fcc and a bcc structure. Amongst that there are more crystalline structures such as the hexagonal closest packed (hcp) structure for example, whose are not further discussed in this work. The deformation mechanism is dependent on the structure the crystal exhibits. Cu exists in a fcc formation, Cr and W in a bcc structure.

Fcc single crystals

The fcc structure is closest packed, the dislocations glide on the closest packed [1 1 1] plains in <1 1 0> direction. Fcc metals posses 12 slip systems. Due to the fact that these slip systems are equal concerning their activation, the dislocations posses several possibilities to move. The main mechanisms in plastic deformation can be retraced to dislocations, twinning and grain boundary sliding [8]. The two dominating mechanisms in single crystals are slip and twinning, whereas for fcc metals the tendency to twin is defined by its stacking fault energy (SFE). Materials with high SFEs like Al, Ni and Cu prefer to deform by slip dislocation accompanied by low strain rate at RT, whereas fcc metals with low SFE like Ag mainly deform by twinning [9].

Bcc single crystals

The deformation structure of bcc metals is way more complex than it is for bcc metals. Therefore it offers a high interest concerning material investigation. The plains of bcc metals are less dense packed then those of fcc metals what leads to different dislocation movement mechanisms. For bcc metals one have to distinguish between two different regions for the mechanical properties. Above the so-called athermal temperature, bcc metals show an almost similar behavior as fcc metals. Below the critical temperature T_C (Fig 2.1) the high Peierl's potential dominate the deformation. Consequential, bcc metals posses a thermal σ_t and an athermal fraction σ^* of the flow stress σ_f, shown in equation (2.1) [10].

$$\sigma_f = \sigma^* + \sigma_t \tag{2.1}$$

The reason for the thermal stress component is the high Peierl's potential of bcc metals, which is almost negotiable for fcc metals since they are closer packet. With increasing temperature, the thermic stress component decreases until T_C is reached. At temperatures above T_C bcc metals then show the same deformation characteristic like fcc metals. The thermal stress component leads subsequently to the characteristic deformation behavior of bcc metals such as strain rate sensitivity and thermal activation of dislocation mobility [11].

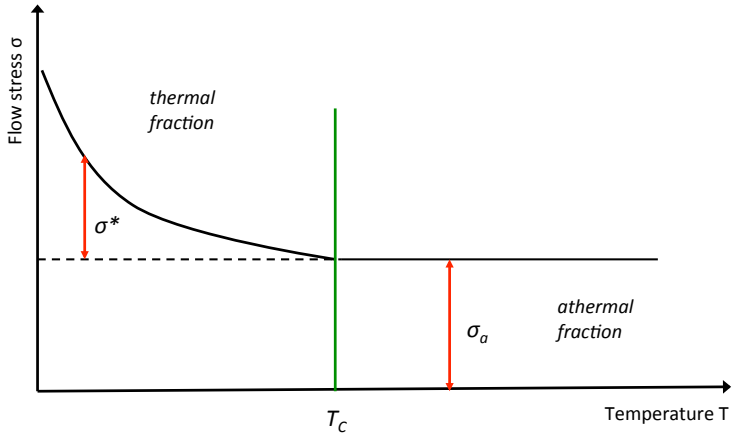

Fig. 2.1: The deformation structure of bcc metals with thermal and athermal fraction

Moreover, the temperature independent contribution to the shear stress arises from dispersed impurities, precipitates and the Snoeck effect [10]. Thus, the critical temperature has no fixed value what yields to different information in literature. Different sources reveal values for T_C of sx chromium between 100°C and 300°C [12–15]. W possesses a T_C of ~800°C [15,16].

2.2. Nanoindentation

Nanoindentation belongs to the depth-sensing material testing techniques and profiles itself through its simple application characterizing a wide range of material properties [18]. It provides several mechanical properties besides hardness such as Young's Modulus, relaxation and creep behavior and strain rate sensitivity [4,19,20]. The application spectrum can be advanced through implying testing methods at different

temperatures [21]. For the indentation testing several different indenter shapes are available. There are cube-corner, conical, spherical and yet the most common one, the Berkovich indenter, which is used in all the following investigations [18]. The following Fig. 2.2 demonstrates a schematic indent. Independent on the kind of force applied on material, the present material shows an elastic and plastic fraction of the deformation. Corresponding to the indentation process, one has to distinguish between the elastic depth h_{elast} and the plastic depth h_{plast}. The maximum penetration depth h_{max} follows from the sum of both. After force removal and pulling back the indenter tip, a part of the material derives back elastically. Moreover, not just the immediate area below the indent is deformed, yet a flattening or curvature around the indent appears. This subsequently falsifies the projected contact area A_c. For calculating the actual contact area, which is essential for measuring hardness via the applied maximum force F_{max} just as it is utilized in conventional micro hardness testing, the contact area has to be corrected. Since for nanoindentation the projected area is not interpreted optically, it has to be calculated using the contact depth h_c, which follows of the actual depth h, minus h_s as shown in Fig. 2.2.

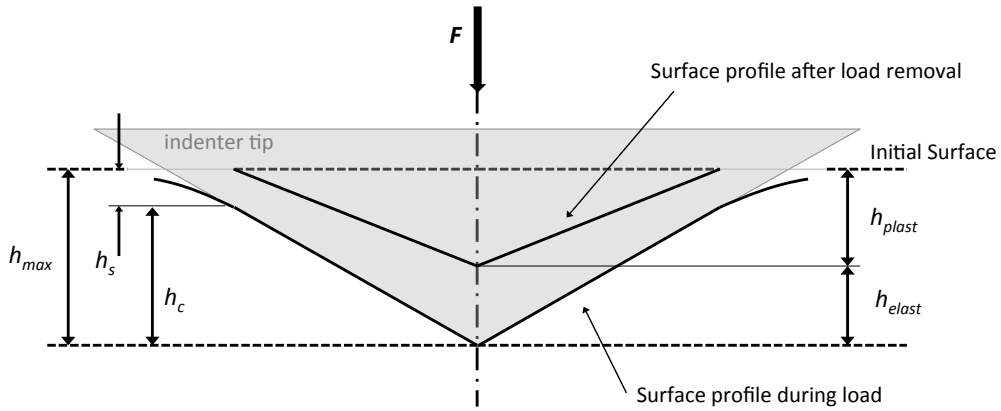

Fig. 2.2: Schematic demonstration of an indent showing the different depth partitions

Since nanoindentation is referred to the depth-sensing techniques, the penetration depth and the applied force on the material through the process of indentation are continuously measured and recorded. For the applied force several modes can be used. The testing program can run load controlled as well a time controlled where the loading rate is the main parameter [22]. There are several more schemes such as the constant displacement rate and the constant strain rate mode [23], which can be implied, yet they are not used during this research and thus not essential for further explanation.

2.2.1. Hardness and Young's modulus

In the year 1992 Oliver and Pharr introduced a method for measuring hardness and Young's Modulus by nanoindentation since instrumented indentation techniques became more and more popular in material testing [4]. The advantage this technique offers profiles itself over conventional microhardness testing, such as Vickers or Brinell where the hardness is calculated through the applied force and the optically measured contact area. This technique avoids imaging the hardness impressing while it uses the load displacement curve as shown in Fig. 2.3 over which the characteristic material parameters can be analyzed [24].

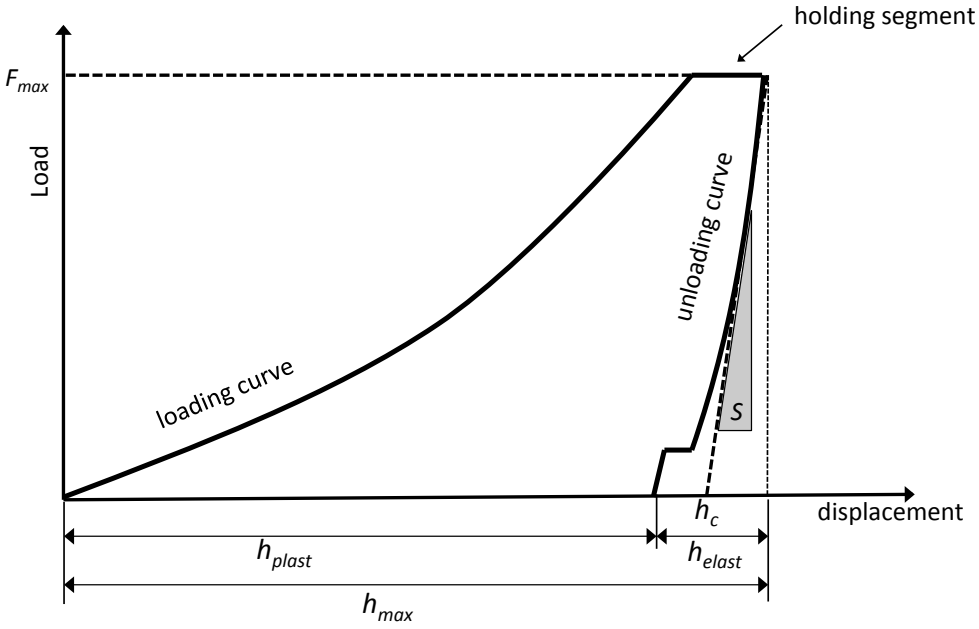

Fig. 2.3: Load displacement curve of nanoindentation testing

This schematic illustration of a displacement curve contains the parameter *F* representing the load and *h* as displacement of the indenter into the surface. As mentioned above, the deformation contains both elastic and plastic partition, whereas during unloading the elastic displacement recovers. Subsequently the elastic behavior of the unloading curve contributes to the Young's modulus analysis. Besides the two main parameters, the maximum load F_{max} and the maximum displacement h_{max}, the calculation further requires the slope of the upper partition of the unloading curve d*F*/d*h*, which represents the elastic unloading stiffness *S*. It expresses the stiffness of the whole system which both can be contributed to the material and the testing equipment.

The unloading curve can be described by the following power function (2.2):

$$F(h) = A \cdot (h - h_f)^q \tag{2.2}$$

A, h_f, and *q* describe the fitting parameters, whereas h_f represents the final depth or alternatively described as remaining plastic depth h_{plast} after the intenter is fully unloaded. The stiffness S is found by taking the derivative of the equation above:

$$S_{tot} = A \cdot q \cdot (h_{max} - h_f)^{q-1} \tag{2.3}$$

Furthermore, the inverse of the stiffness offers the compliance C_{tot}, which again, based on S_{tot}, contains both the compliance of the sample C_s and the machine or frame compliance C_f, which is explained in the following chapter. Subsequently the machine compliance requires to be subtracted from C_{tot} after equation (2.4):

$$C_s = C_{tot} - C_f \tag{2.4}$$

The inverse offers now the stiffness after equation (2.5):

$$S = \frac{1}{C_{tot} - C_f} \tag{2.5}$$

Furthermore, Oliver and Pharr made the assumption that the elastic depth h_s is a function of F_{max}, *S* and a constant ε, which depends on the indenter geometry ($\varepsilon_{Berkovich}$ = 0.75) [24]. Thus, equation (2.6) follows:

$$h_s = \varepsilon \cdot \frac{F_{max}}{S} \tag{2.6}$$

Subsequently the contact depth h_c derives from subtraction of h_s from the maximum depth h_{max} after the final equation (2.7), which is universally used in all common nanoindentation tests:

$$h_c = h_{max} - \varepsilon \cdot \frac{F_{max}}{S} \tag{2.6}$$

Since the impression of the indenter is not imaged, a so called "area function" A_c has to be defined, which describes the projected area dependent on the contact depth h_c. Oliver and Pharr suggested following polynomial equation as correlation between A_c and h_c:

$$A_c(h_c) = C_1 \cdot h_c^2 + C_2 \cdot h_c + C_3 \cdot h_c^{\frac{1}{2}} + C_4 \cdot h_c^{\frac{1}{4}} + \cdots + C_9 \cdot h_c^{\frac{1}{128}} \tag{2.7}$$

Whereas C_1 = 24.5 for an ideal Berkovich indenter and $C_2 - C_9$ are coefficients correcting deviations from non ideal indenter geometry. The area function including the coefficients for deviations has to be accurately determined by independent measurements on known material and is part of my investigation in a later chapter. Subsequently the hardness can be estimated through the indenter load F_{max} and the area function A_c through following equation:

$$H = \frac{F_{max}}{A_c} \tag{2.8}$$

Now, the Young's Modulus can be estimated through the reduced modulus E_r in equation (2.9) by taking in account that the elastic displacements appear both in the sample and the indenter:

$$E_r = \frac{\sqrt{\pi}}{2 \cdot \beta} \cdot \frac{S}{\sqrt{A_c}} \tag{2.9}$$

This equation expresses a very general relation and can be applied for any axisymmetric indenter. β is a geometry factor, which in the original methods has been set as unity and was used to take the deviations for stiffness caused by the absence of axial geometry in all pyramidal indenters into account. Considering that the used Berkovich indenter tip with its pyramidal shape is not a body of revolution, $\beta_{Berkovich}$ obtains the value of 1.034 [25]. Due to the instrumental setup can be seen as a series of springs, following equation (2.10) can be applied, considering the Young's modulus E_i and the Poisson's ratio ν_i of the indenter and ν_s as Poisson's ratio of the sample material are known (E_i = 1141 GPa, ν_i = 0.07) [24], [26]:

$$\frac{1}{E_r} = \frac{(1-\nu_i)^2}{E_i} + \frac{(1-\nu_s)^2}{E_s} \tag{2.10}$$

2.2.2. Calibrations

Nanoindentation is a very sensitive material testing method and the measuring is influenced by many factors as shown above. To minimize the errors associated with the frame compliance C_f and the area function A_c, it is essential to calibrate the nanoindenter and correct the measured values on the basis of investigations on a homogenic material with known material properties. In general, fused silica is used as calibration material (H = 8.85 GPa, E = 69.6 GPa, ν = 0.17) [27]. Furthermore, the probability of fused silica showing falsifying phenomena such as "pile-ups" or "sink-ins" is very unlikely due its low E/H ratio [18].

2.2.2.1. Machine compliance

As the measured displacement of a depth sensing instrument results from the sum of the actual displacement into the specimen and the additional displacement associated with the instrument, the machine compliance requires to be analyzed properly since its influence increases proportional with increasing forces. The most common factors that contribute to the machine compliance are the transducer itself, the indenter sample and the sample mounting, since these components represent the sequence of the entire testing device [22]. For a sufficient calibration it is required to perform at least 20 indents at different depths, covering the load range, which on the investigated material is applied.

2.2.2.2. Area function

A Berkovich indenter corresponds to the shape of a three-sided pyramid with triangular faces, the resulting area of the impression derives from its geometrical constant C_1 of 24.5. This presumption looses its validation with decreasing indentation depth since the cone end deviates from its perfect shape to a spherical shape with varying degrees. The probe calibration compensates this non-perfect probe shape and can be performed with the machine compliance calculation. However, the minimum load should be small enough to ensure that the contact depth is below the lowest contact depth desired on the investigated samples [18,22]. With the obtained values and considering the elastic modulus of fused silica to be 69.6 GPa, the projected area can be calculated transforming

equation (2.8) and (2.9). The calculated area is plotted as a function of the contact depth h_c, as shown in Fig. 2.4. This typical area function calibration software was provided by the manufacturer of the testing device. This curve then can be fitted to the polynomial shown in equation (2.7). When performing deep indents, the first term will gain significance since the pyramidal shape of the tip prevails.

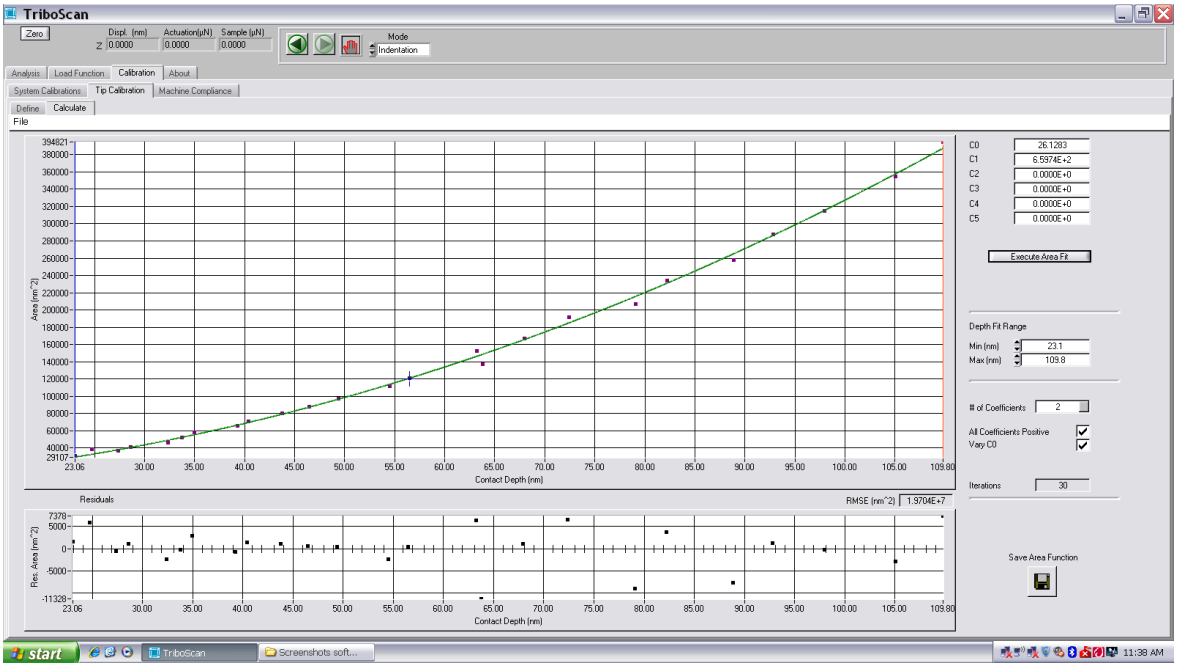

Fig. 2.4: Plot of the projected area versus contact depth to calculate the area function

2.2.3. Pile-ups and Sink-ins

In the context of indentational material testing the analysis of the projected area possesses a major role since the hardness and the elastic modulus of the investigated material is estimated through the applied force and the stiffness. For both, conventional hardness testing techniques and nanoindentation methods, whereby the area is assessed optically for conventional testing and calculated through the area function as suggested by Oliver and Pharr [24] for nanoindentation methods respectively, the different plastic behavior of the material has to be considered. The most significant phenomenon introducing an error to the area function and the correlated hardness is the appearance of so called “pile-ups” and “sink-ins” as shown in Fig 2.5. Bulging around the indent can be identified as pile-ups and sink-ins show a sinkage at the edge of the imprint. Which

kind of formation actually occurs is dependent on the *E/H* ratio and the strain hardening properties of the material. Materials with low strain hardening potential such as work-hardened metals tend to pile-up. The plastic deformation during the impression takes place in immediate contact to the indenter tip. The material has to be displaced upward and generates a pile-up [18]. The opposite reaction is attributed to materials with high strain hardening potential such as well-annealed metals or single crystals, which posses a very little initial dislocation density and a small *E/H* ratio. The impression creates dislocations at the right contact with the material, which leads to an instant increasing of the dislocation density and thus to work hardening of the surface. The further deformation has to take place in a lower region of the material, which leads to a sink-in.

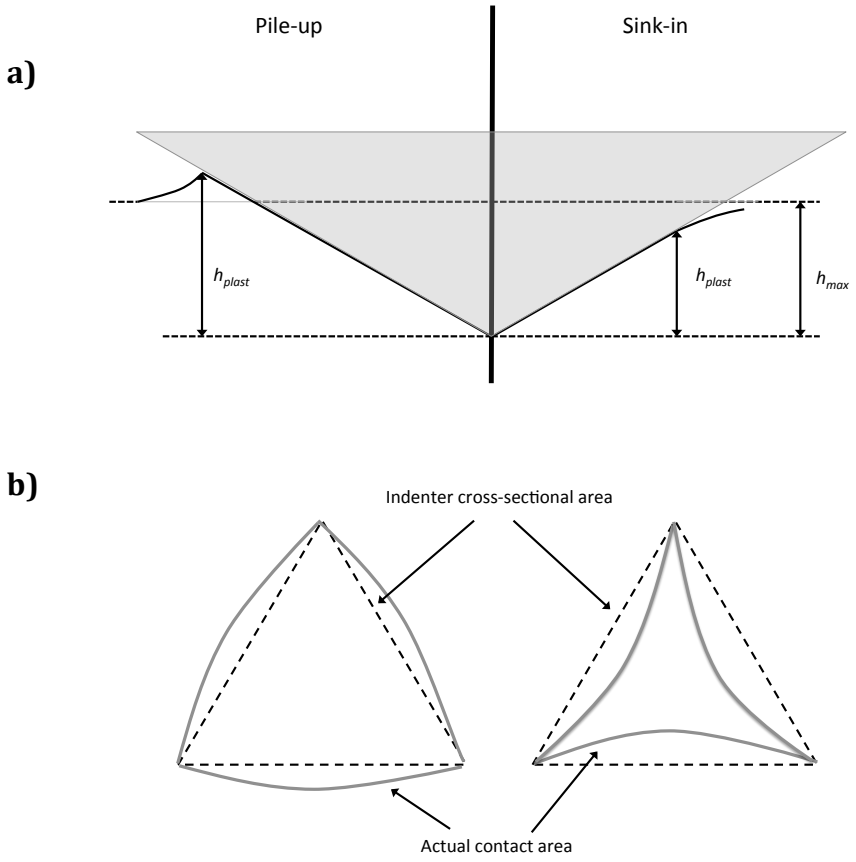

Fig. 2.5: Projections of pile-ups and sink-ins. a) cross-sectional projection. b) plan view projection.

Both phenomena lead to a misinterpretation of the area and thus to inaccurate values for hardness and Young's modulus. Pile-ups generate a larger area and result in an under-estimation of the hardness. The projected area of materials showing sink-ins is underestimated, consequently the hardness is overestimated. To take these aspects into

consideration, imaging of the surface for each individual indent with Atomic Force Microscopy (AFM) would be required [28,29]. These efforts would exceed the scope of this thesis, yet selected samples were analyzed for representative purpose.

2.2.4. The Indentation Size Effect and its analysis

The main focus of material science is to investigate the physical and chemical correlations of materials and to study its influence on the material behavior. In this context, length scales and their interactions play a major role. Departing from the atomistic scale, atoms, their size and distance coming to the microscopic scale regarding grains and their dimensions, material behavior can be referred to certain and specific length scales [30]. Yet another element becomes relevant when changing the dimensional method of view: a size dependent change of properties. This size-scale effect can be defined as a change in material properties (mechanical, electrical, optical or magnetic) what can be referred to a dimensional change of an internal feature or structure or in the general physical dimensions of a sample [31]. Brenner et al. discovered 50 years ago a large yield strength increase in tensile testing of single crystal metallic whiskers with decreasing diameters [32]. Basic processes of plastic deformation are immensely affected by the decrease of the external dimensions of the sample, although according to conventional theories of plasticity, the mechanical properties are assumed to be constant and independent of material length scale. This presumption would provide that the flow stress at any point in a solid is exclusive dependent on the present strain and independent of the strain gradient. In the special context of indentation testing techniques this fact would provide that the measured hardness is not related to the indentation depth since the hardness is calculated through the applied force divided by the projected area as shown in equation (2.8). However several experiments have shown that with decreasing indentation depth, the hardness of the sx and coarse-grained material increases. It seems to be reasonable to reduce the increasing hardness to sample preparation artifacts such as deformation structure due polishing or the formation of oxide layers. Both would lead to a strengthening of the surface, either through a chemical transformation or through work hardening. Nevertheless even in accurately prepared metallic samples this phenomenon appeared and is shown in Fig. 2.6, where hardness is plotted over the indentation depth.

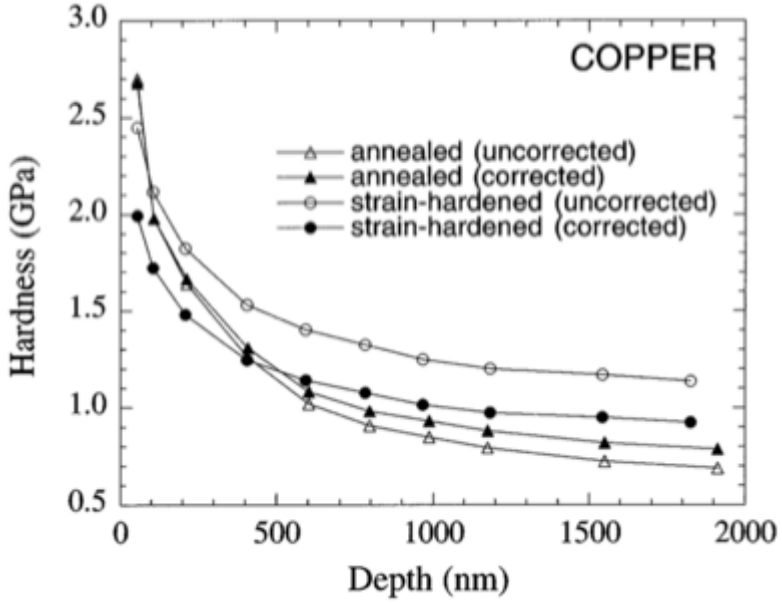

Fig. 2.6: Depth dependence of cold worked polycrystalline and single crystal Cu [33]

An explanation for the ISE was first found by Ashby in 1970 [34] and then advanced by Fleck and Hutchinson (1993, 1997) [5] by the assumption that the for deformation necessary flow stress is not just strain but as well strain gradient dependent. Nix and Gao (1997) described the strain gradient plasticity to be retraced to the coexistence of statistically stored dislocations and geometrically necessary dislocation. Statistically stored dislocations are compulsory present in the material whereas geometrically necessary dislocations occur to carry the plastic deformation induced by the indenter forced into the surface as shown in Fig. 2.7.

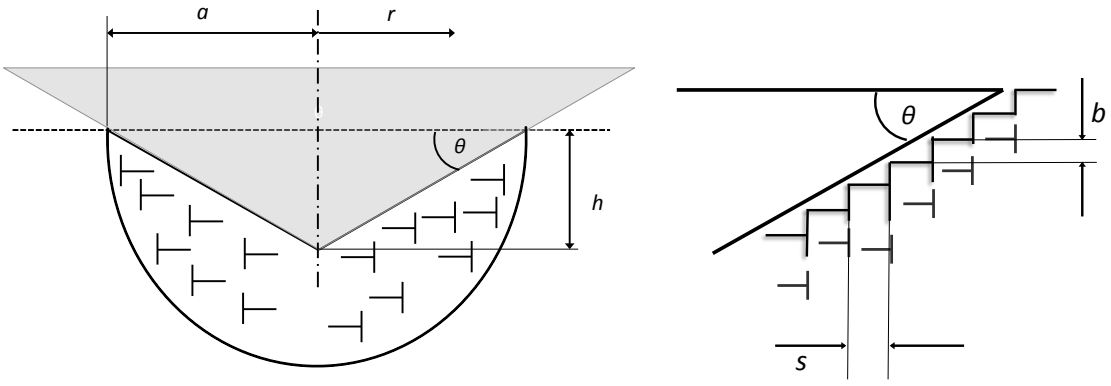

Fig. 2.7: Geometrically necessary dislocations created by a rigid conical indentation. The dislocation structure is idealized as circular dislocation loops.

To explain the increasing hardness with decreasing indentation depth, Nix and Gao described a correlation of how the density of the geometrically necessary dislocations

and the occurring strain gradient in the material influence the plasticity. To describe the size effect based on their strain gradient plasticity model they developed following equation (2.11), where *H* represents the hardness at a certain indentation depth (*h*), H_0 is the macroscopic hardness of the material and *h** characterizes an internal length scale describing the increase of the hardness with decreasing depth.

$$\frac{H}{H_0} = \sqrt{1 + \frac{h^*}{h}} \tag{2.11}$$

Although Nix and Gao's model still is broadly used to analyze the ISE, yet several improvements have been established. Investigating the size effect on MgO, Feng and Nix found that the previous model overestimates the hardness for indentation depth less than 200 nm and presented a new model by defining an improved plastic zone [35]. Kim et al. enhanced the ISE model including the influence of the tip bluntness based on the GND theory [36]. Liu and Ngan showed in their work how polishing methods, especially mechanical sample preparation are related to depth effects on the hardness of the crystals [37]. Abu al-Rub advanced the previous Nix-Gao model by a material specific correction of the internal length scale and showed that weaker samples exhibit higher ISE. Subsequently the size effect is expected to be not only influenced by prior dislocations and but as well by additional work hardening that occurs during indentation [38]. Rester et al. investigated the deformed volume below nanoindentations in sx Cu. They presented an apparent indentation dependent change in the structure of the deformation zone, which is linked to a variation in the deformation mechanism as they found huge orientation changes for large imprints, whereas for shallow indentations the appearing misorientation was only minor. This leads to the necessity of the distinction between different length scales at different indentation depths [39].

To analyze the ISE in the present material on behalf of the indentation tests, the described Nix and Gao model is used. The hardness values *H* at the corresponding depths *h* are known. Subsequently the internal length scale *h** as well as the macroscopic hardness H_0 can be calculated by transforming equation (2.11) to following equation (2.12). With plotting the values of H^2 over *1/h*, the linear regression of this plot provides H_0 in the form of the y-interception of the regression line. To generate the Nix-Gao plot,

in which the linear depth dependence of the hardness is shown, H^2/H_0^2 is consequently plotted over the reciprocal values of the corresponding depths *h.* The internal length scale *h** now can be enabled through the slope of the regression line.

$$H^2 = H_0^2 + H_0^2 \cdot \frac{h^*}{h} \tag{2.12}$$

2.2.5. Explanation of the size effect and differences between bcc and fcc metals

One explanation for the dimension referable size effect is the *dislocation starvation hardening* as discussed by Nix et al. [40]. The dislocations especially in small-scale single crystalline materials leave the crystal faster rather then multiplying. This behavior requires a continual nucleation of dislocation during the course of deformation resulting a higher flow stress compared to bulk material. Volkert and Lilleodeen suggested that dislocations are lost through the sample surface resulting a decrease in the dislocation density. Subsequently the applied stress has to be increased to create further plasticity. This accounts for the increasing yield stress and strain hardening behavior [41]. These phenomena mainly explain the dimensional based size effect of fcc materials. They show almost temperature independent dislocation mobility of screw and edge dislocations due to the fact that they do not posses a thermal and athermal fraction as previously explained. Bcc metals show different dislocation interactions. The screw dislocations move by thermally activated kink pair nucleation and motion. Subsequently below the material specific T_c the mobility of screw dislocations is smaller than of edge dislocations [6,21]. This leads to the assumption that in bcc metals non-screw dislocations move much faster than screw dislocations [43]. Weinberger and Cai showed that the slower screw components are retained during deformation and are able to cross-slip to form a loop, which again divides into two separate dislocations. As leaving the specimen, they release a loop that eventually divides into two separate dislocations. This results in the multiplication of dislocation with increasing effect on decreasing specimen sizes [44].

In summary, size effects, which are specimen dimensional related, both in fcc as bcc metals exist and occur both in the context of pillar testing as well as in nanoindentation

experiments. Yet it seems that size effects differ in their occurrence concerning their crystalline structure. Moreover, leaving ambient testing conditions and examining the material behavior at elevated or reduced temperatures, size effects change in their quantity. Franke et al. discovered a decrease of the indentation size effect with increasing temperatures in the context of nanoindentation of fcc single crystals [45]. Bcc metals seem to behave different when tested below the critical temperature, which manifests the major difference between bcc and fcc. Schneider et al found that the critical temperature has a strong influence on the deformation morphology of metals. A larger T/T_c ratio, meaning a decreasing gap between test temperature and critical temperature can be associated with higher thermal activation and thus higher mobility of screw dislocations. At one material specific T/T_c ratio a condition is reached where screw and edge dislocations have equal mobility and thus lead to similar size effects between fcc and bcc metals [17]. Up till now the majority of studies concerning size effects focus on fcc materials, investigations on bcc size effects are still in the fledging stages. Maier et al. observed in an unpublished study as comparing indentation size effects of sx and ultra fine grained (ufg) materials that bcc metals show a weaker size effect with decreasing temperatures below their critical temperature. Then above T_c bcc materials exhibit similar size dependence as fcc metals, the size effect declines with increasing temperatures. The temperature dependence of the size effect of bcc and fcc metals according to Maier's investigation is delineated in Fig. 2.8 [46].

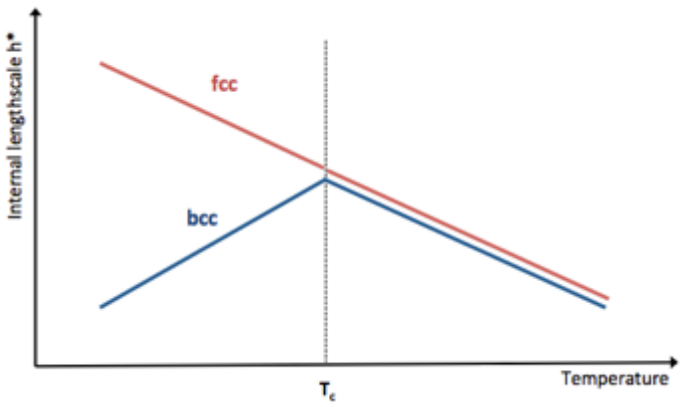

Fig. 2.8: Temperature dependence of the size effect of fcc and bcc materials

2.2.6. Transition from elastic to plastic deformation – “pop-in” phenomena

In the context of deformation, every material shows a more or less extended elasticity until the plastic deformation begins. In a typical load displacement curve this transition reveals itself with an apparent step in the loading curve as shown in Fig. 2.10. This characteristic “pop-in” load can be attributed to the nucleation of dislocations. Due to the abrupt activation of the plastic deformation the depth is suddenly emerged while the load stays constant. Although the event of the dislocation nucleation and so the occurrence of pop-ins in the material mainly is referred to its shear stress, its influenced by many factors and thus part of many research investigations. The lattice structure defines the preferred slip planes for the dislocation movement. Bcc metals obtain a higher number of available slip systems compared to fcc metals, thus they exhibit a larger number of displacement bursts in the early stages of deformation [47]. Furthermore, the tip geometry influences the displacement burst. A conical indenter distributes the load over a larger area due to the large radius of the tip. The possibility to activate a present dislocation in the material is subsequently more likely compared to a Berkovich indenter that has a negligent small tip radius. Shin et al. [48] have shown on the basis of different tip radii of conical indenters to actually differentiate between two regimes in the incipient plasticity. Assuming the tip radius is responsible for the involved volume, small tip radii cover a smaller volume and thus the incipient plasticity is dominated by the nucleation of new dislocations. Larger tip radii involve a larger volume and the deformation is referred mostly to the activation of present dislocations.

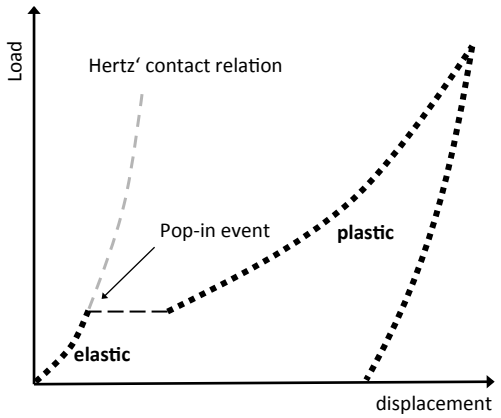

Fig. 2.9: Typical load-displacement curve showing the pop-in event

A Berkovich indenter obtains the shape of a three-sided pyramid with triangular faces. The cone end is not perfectly sharp but can be assumed to be blunt to varying degrees [49]. This fact allows approaching the elastic deformation before the pop-in appears by the Hertzian contact relation (2.13), which bases on the contact between a sphere and flat surface. The apparent progression is illustrated in Fig. 2.10 [50].

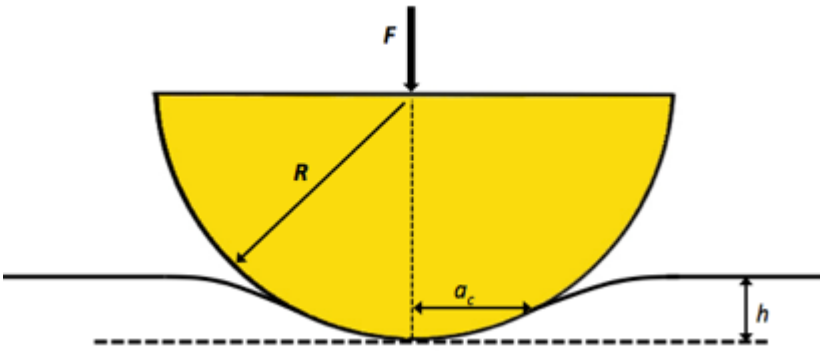

Fig. 2.10: Schematic illustration of the Hertzian contact between a sphere and an elastic flat surface

$$F = \frac{4}{3} \cdot E_r \cdot R^{1/2} \cdot h^{3/2} \tag{2.13}$$

F represents the indenter load, E_r the reduced modulus, *R* the indenter tip radius and *h* stands for the elastic contact depth. This equation allows calculating the tip radius from a known or measured reduced modulus by evaluating the elastic curve progression. The maximum stress at the pop-in events is recognized as the theoretical shear strength of the material and can be calculated on the basis of the detected tip geometry and the reduced modulus according to equation (2.14) and (2.15):

$$p_m = \left(\frac{6 \cdot P \cdot E_r^2}{\pi^3 \cdot R^2}\right)^{\frac{1}{3}} \tag{2.14}$$

$$\tau_{max} = \frac{G}{2 \cdot \pi} = 0.31 \cdot p_m \tag{2.15}$$

p_m is the mean pressure at the moment the pop-in appears and τ_{max} is the theoretical shear strength of the material assuming that a homogenous nucleation of dislocation occurs [50].

2.2.7. Nanoindentation under non-ambient conditions

Most of the studies concerning nanoindentation deal with material testing around room temperature. Due to the fact that the scope of application of materials experiences an immense enlargement, material testing beyond room temperature becomes inalienable. Yet, nanoindentation under non-ambient conditions is afflicted with enormous challenges. Lucas and Oliver were the first to publish in 1995 their microscale studies on Indium from 75°C to -100°C [21]. Suzuki and Omura published their study in 1996 on Silicon wafers on elevated temperatures up to 600°C using nanoindentation [51] and experienced challenging issues concerning thermal drift due to the fact that just the sample was heatable and cooled down by the approaching tip. Schuh et al. dedicate a whole investigation on those issues referred to nanoindentation on non-ambient conditions, in particular testing above RT [52]. As experienced by Suzuki and Omura, the rapid heat transfer between a cold tip on a heated surface is accompanied by thermal extension of the tip, transient thermal contraction of the sample on the immediate contact point, and additionally elevated electronic drift in the case the sensing devices behind the tip experience higher temperatures. An equilibration of the temperature between tip and surface can be accomplished by customized heating elements both for tip and sample [53]. An additional procedure is to bring tip and specimen for a designated time into contact. After assuring an entire temperature equilibration, the sample testing can be initiated. Modern nanoindentation systems perform a drift analysis ahead (HYSITRON®) or after (Agilent®) testing to correct the obtained values to the drift remaining despite equilibration. Despite Schuh et al.'s investigations that the change of the tip geometry including area function with increasing temperatures can be neglected, it has been shown that further thermally accelerated processes such as oxidation do change the tip structure. Wheeler et al. demonstrated that relatively rapid oxidation including erosion accelerates especially at temperatures above 450°C in ambient air, recommending that conditions with very low levels of oxygen rather those of commercial purity argon are necessary to avoid diamond erosion [54]. In a further investigation Wheeler showed that at certain temperature one even has to concern about chemical interaction between tip and specimen and recommended the usage of tungsten carbide as indenter material to avoid chemical reactions [55]. In the context of the present investigation with indenting at cryogenic temperatures, chemical reactions between

surface and tip can be neglected. Yet, thermal drift plays a mayor role due to operating beyond ambient conditions. Operating on the cryogenic in situ micro compression of Sn pillars, Lupinacci et al. performed an extended contact time between specimen and tip ahead of their experiments to ensure a total equilibrium between both [56]. Another problem dealing with a high temperature difference between sample and surrounding environment is the constant heat conduction from the environment (or the chamber in which the testing takes place) to the sample stage [57]. And last but not least, all cryogenic testing units require a liquid nitrogen flow. This stream subsequently causes vibrations to a certain level and evokes noise in the sensing devices recording the measurement.

Subsequntly, all experiments beyond ambient temperatures are subject to several challenges. A major role of any investigation working beyond room temperature is to reduce these problems to enable reliable results.

3. Experimental setup

The investigations for the present work were performed on single crystalline Cr, Cu and W, which were exclusively supplied by “Mateck GmbH” in rod-shape. According to the manufacturer’s data sheet they were produced with 99.999% purity and 2° orientation accuracy. The Cr bar was manufactured in a 10 mm thick bar, W in 15 mm and Cu in 20 mm [58]–[60]. A diamond wire saw was used to withdraw 1 – 1.5 mm thick disks from these rods. These disks then again were minimized by cutting into four (Cr), respectively six (W) and eight (Cu) pie slices to provide an appropriate sample size for the application and to retain several spare samples.

3.1. Properties of the provided single crystals

The mechanical properties of the provided single crystals are listed in table 3.1. Cu represents the fcc metal group, the single crystal was fabricated through the Czrochralski process. Cr and W both occur in a bcc lattice structure. The sx were manufactured in a float zone process.

Table 3.1 Properties of the provided single crystals [14,58–62]

	Cu	**Cr**	**W**
Atomic number	29	24	74
Standard atomic weight	63.546	51.996	183.85
Density	8.96 [g cm^{-3}]	7.15 [g cm^{-3}]	19.3 [g cm^{-3}]
Melting point	1083 [°C]	2130 [°K]	3680 [°K]
Thermal conductivity	401 [W m^{-1} K^{-1}]	93.7 [W m^{-1} K^{-1}]	174 [W m^{-1} K^{-1}]
Bulk tensile strength	220 [MPa]	103 [MPa]	550 [MPa]
Young’s modulus	100 [GPa]	279 [GPa]	411 [GPa]
Poisson’s ratio	0.343	0.21	0.28
Critical temperature	-	453 [K]	800 [K]
Theoretical shear stress	3.64 [GPa]	18.3 [GPa]	25.6 [GPa]
Hardness	0.49 [GPa]	0.106 [GPa]	3.60 [GPa]
Lattice type	fcc	bcc	bcc
Fabrication	Czochralski	Float zone	Float zone

3.2. Sample preparation

Due to the very sensitive testing conditions and the massive influence of the sample surface, an accurate preparation of the samples is essential. The single crystalline samples were prepared at the metallographic laboratory at the Erich Schmid Institute in Leoben according to table 3.2.

Table 3.2 Sample preparations, methods and steps

Preparation step	Cr	Cu	W
Mechanical grinding	- UltraPrep 15µm - UltraPrep 9µm - UltraPrep 6µm - UltraPrep 3µm - UltraPrep 1µm	- SiC 320	- SiC 320 - SiC 500 - SiC 800 - SiC 1200 - SiC 2000 - SiC 4000
Mechanical polishing	- MD-Chem: OP-S 0.04µm + H_20_2	- MD-Largo 9µm - MD-Dac 3µm - MD-Nap 1µm - MD-Chem: OP-S 0.04µm	- MD-Dac 3µm - MD-Nap 1µm - MD-Chem: OP-S 0.04µm + H_20_2
Electrolytic polishing - Temperature: - Electrolyte: - Voltage: - Time:	 RT A2 24 V 120 s	 4°C D2 8 V 30 s	 RT F1 26 V 120 s

3.3. Microstructure investigation

The available single crystals were manufactured in a specific crystalline orientation. In order to evaluate information about the possible variation of the actual orientation, the likely presence of small angle grain boundaries and pores, EBSD imaging was used. The EBSD detector is connected to an electron microscope (SEM), in which the scanning apparatus is positioned. The functional principle behind an electron microscope is the interaction between a high energetic electron beam with the atoms of the sample's crystalline layer. Those backscattered electrons, which comply Bragg's law generate a characteristic pattern at the nearby located phosphor screen. A CCD camera enables to

plot the pattern at a computer and analyze the characteristic pattern. On basis of the pattern a conclusion of the crystalline orientation can be made [63]. The orientations are usually illustrated in inverse pole figures as shown in Fig. 3.1 in which the direction can be readout on the basis of crystalline coordinates. The used SEM was a “Gemini Leo 1525” located at the Erich Schmid Institute in Leoben.

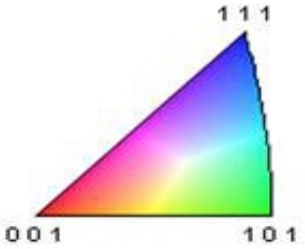

Fig. 3.1: Inverse pole figure with colored characteristic crystalline orientation of the crystal unit cell

The parameters used for the EBSD imaging were an acceleration voltage of 20 kV, an aperture of 20 µm and a high current mode to enable a high intensity of back-scattered electrons. First the single crystals were coarsely scanned on an area of 3 x 3 mm with a step size of 2 µm to generate a rough overview over the surface and show a possible variation of the actual orientation and small angle grain boundaries. To reveal the actual orientation in a high resolution, the surface then was scanned on a 10 x 10 µm area with a step size of 0.1 µm.

3.4. Microhardness measurements

In order to gain additional information on a micromechanical level of the single crystals and to be able to refer the values to the expected nanomechanical properties, microhardness measurements were performed. 10 indents per sample were conducted. Subject to the regulation of hardness testing, a sufficient spacing between the impressions of at least the 4 times the diameter of an indent was maintained. The indentation load was adjusted to the theoretical hardness of the materials. The used loads were 100 g (HV 0.1) for Cu, 300 g (HV 0.3) for Cr and 500 g (HV 0.5) for W. The microhardness measurements were performed on a “BUEHLER Micromet 5100” located at the Erich Schmid Institute in Leoben.

3.5. Nanoindentation

The basis of the present thesis are nanoindentation experiments in order to gain information about the material properties such as hardness, Young's modulus and the ISE and especially its temperature dependence. Following, the experimental setup, necessary preparations and techniques as well as the used parameters for the different test are explained. The data processing and visualizing was conducted with the manufacturers software "HYSITRON TriboScan 8®" and Microsoft Excel®.

3.5.1. Experimental setup

The used nanoindentation device was a "HYSITRON PI-85®", which was applied in the SEM/FIB installation "FEI Quanta 3D FEG®". The facility was located at the Biomolecular Nanotechnology Center (BNC) at Stanley Hall, University of California, Berkeley. The main testing setup consists of the indenter, which is composed of an XYZ transducer on which the tip can be mounted and a sample holder. Furthermore, a cooling unit, manufactured by Hummingbird Scientific, advanced the indenter system. The cryogenic system allows cooling down both the sample and the tip simultaneously in order to minimize thermal drift [56]. A schematic illustration and an image of the cryogenic setup of the indenter system are shown in Fig. 3.2.

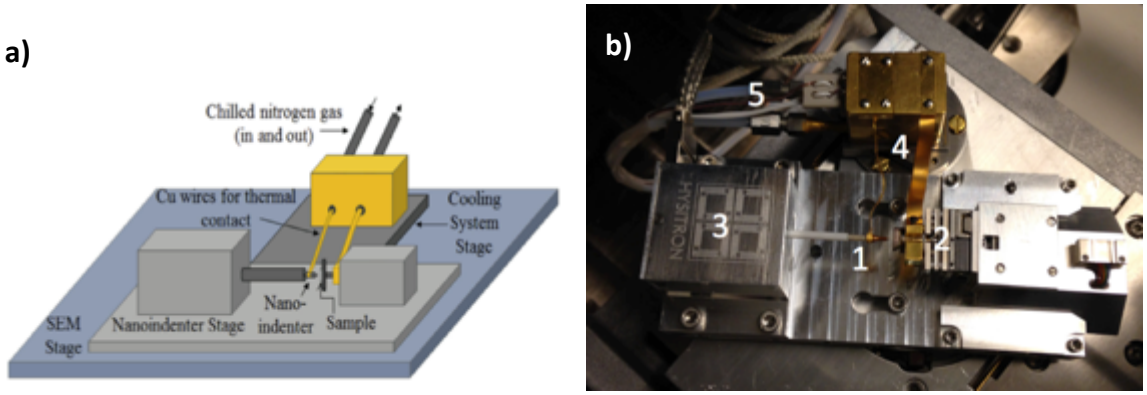

Fig. 3.2: Cryogenic testing application. a) Schematic of the cooling and the indentation stage [56]. b) Image of the cryogenic setup with cooled nanoindentation tip (1), sample holder (2), XYZ transducer unit (3), wiring for thermal contact (4) and nitrogen supply unit (5)

The cryogenic nanoindentation setup was exclusively manufactured to be applied in a SEM/FIB unit. The high vacuum provides an inert atmosphere and avoids chemical

reactions such as oxidation of the sample surface, which would lead to non-representative results. Besides that, the vacuum diminishes the formation of ice on the cooled parts of the stage and surface. The electron microscope displays the position of the tip in reference to the sample surface and allows to image the processes during indentation (Fig 3.3). Ahead of the experiments carried out with the HYSITRON PI 85® in Berkeley, the single crystals were tested additionally on a nanoindenter device with integrated continuous stiffness measurement option (CSM), the Keysight G200 located at the ESI in Leoben. These experiments, all carried out at room temperature should provide first reference values as support and orientation for the calibration at the PI-85 Berkeley.

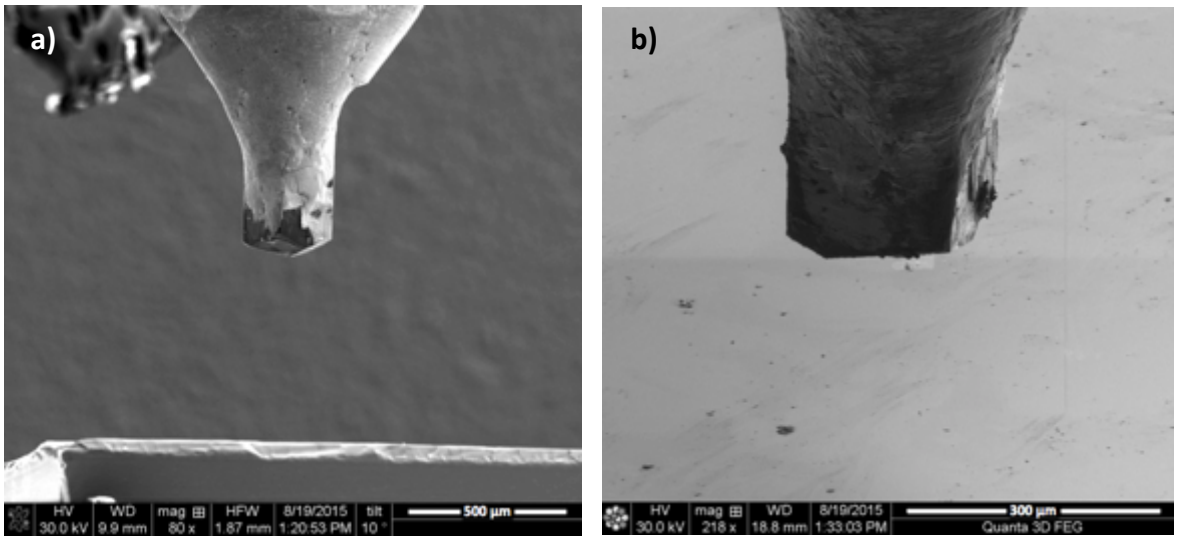

Fig. 3.3: a) SEM and b) FIB image of the tip above the surface of fused silica

3.5.2. Preparation for nanoindentation

For representative examination conditions, a careful assembling of the whole testing setup was required. In order to provide proper imaging via SEM, all examined samples have to be conductive. Due their metallic profile, the tested single crystals provided a good electrical conductivity and thus did not demand any further preparation. However for the calibration sample, fused silica a gold coating was necessary to allow a proper imaging in the SEM. Before applying the cold covering, the relevant area for the calibration indents was protected with a copper tape in order to avoid falsifying gold particles on the surface. Then the extra-high voltage (EHT) was lowered to minimize a blurred imaging of the surface through remaining electrical charge processes of the

sample. Furthermore, a thermocouple was welded on the sample holder in order to detect the actual temperature during testing. The first investigations showed a constant temperature difference of 12°C between the sample and the chill unit. To avoid additional compliance to the experimental setup and a supplemental heat transfer to the sample, the thermocouple was removed after the first test. Subsequently, the temperature of the chill unit was taken and then subtracted by the temperature difference of 12°C. For the sake of simplicity, the listed temperatures in this thesis are corrected to actual sample temperature. Then, the sample was glued onto the sample holder with silver paste, which provides both good thermal and electrical conductivity. The Berkovich tip was then carefully mounted on the transducer and the wire for the thermal contact of the tip was screwed to the chill unit. Care was given to attach the wire tensionless in order to avoid falsifying pre-stresses. Then the copper plate on which the sample was attached was fixed close in front of the tip and the thermal contact wire was connected to the chill unit. Once the SEM chamber had reached a vacuum condition, the indentation stage had to be moved with the control software in front of the SEM and FIB detectors in order to display both tip and sample in different angles on a computer screen. For the cryogenic tests, once the heat exchanger started initiating the cooling, a minimum waiting time of an hour was adhered before starting the experiments to provide thermal equilibration between the sample and the heat exchanger.

Prior to the nanoindentation experiments on the single crystals, the calibration on fused silica was performed. For a sufficient adjustment it is required to execute at least 20 indents at different depths, covering the load range, which on the investigated material is applied. Since the tested materials offer a wide variety concerning their material properties for the actual investigation 50 indents were necessary to ensure that the calibration values are effective for each material. To calculate the machine compliance with the obtained values, a fitted plot is generated displaying the inverse of the stiffness S_{tot} versus the inverse root of F_{max}. The Y-axis intercept of the graph demonstrates the machine compliance, which can be applied for further calculations.

3.5.3. Experimental parameters

The main focus of this thesis is held on the investigation of the Indentation Size Effect and its temperature dependence. With decreasing indentation depths, increasing hardness is observed. To examine this effect, a testing procedure was developed including a set of different loads. The HYSITRON® software offers several different examination programs including load as well as displacement controlled force application on the sample. The displacement-controlled mode would rather be suitable to adjust the required indentation depth steps. However the first investigations have shown that the software primarily operates force controlled and then replies with the encountered depth and the correlating force. Due to the fact that this mode is controlled via a series of regulation, the force- controlled application is rather appropriate since it displays the actual force and correlating values without regularization operation. The maximum force of the cryogenic HYSITRON® indenter was limited to 10 mN. Thus, all single crystal samples were tested by an analogous testing program starting from the maximum applicable force of 10 mN. Though, Cu was tested starting from a maximum force of 6mN due to the fact that the area function for higher forces than 6mN was not implementable on Cu. The displacements at theses forces were very high. Usually the first term of the area function (C_0 = 24.5) should dominate at these displacements and compensate for the fact that the fused silica did not cover these depth ranges. Nevertheless the obtained hardness values did show an unexpected progress for which no correction could be found. The force subsequently was reduced in steps successively to provide different indentation depths in order to examine the size effect. When generating the load program, it is important to apply the same loading *(t_{load})* and unloading time *(t_{unload})* for all indents. This provides a constant rate of loading $\dot{F}/F$ and leads to a constant strain rate $\dot{\varepsilon}$ [64]. Another important component to take into account is the so-called dwell time *(t_{dwell})*, which should be constant for all tests and shortened in order to minimize drift. The load-time schedule for the indentation tests was identical for both all materials and different temperature levels. Both t_{load} and t_{unload} were 15 s, the applied t_{dwell} was 3 s. Indents at five (W) to eight (Cr) different load levels were performed, up to ten at each load level to take potential deviations into account. The impressions were processed at two different temperature levels, the first set was performed at room temperature, the second at the minimal attainable temperature, which was around -150 ± 3°C.

4. Results

4.1. Microstructure

To provide information about the microstructure, EBSD investigations were carried out to detect the orientation of the single crystals. The crystalline direction of the Cu single crystal was identified to be close to [1 1 2] as shown in Fig. 4.1. The Cr single crystal was provided in an [0 0 1] orientation, which could also be detected by the EBSD scan. The slight deviation from its declared orientation can be referred to an inclined cutting or to an oblique mounting to the stage. The direction of the W single crystal could be analyzed as [1 0 1], which accords with the manufacturer's data. The small divergence from its assigned orientation again can be referred to cutting or mounting issues.

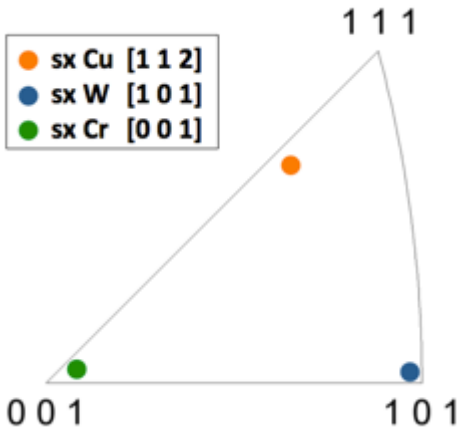

Fig. 4.1: Inverse pole figure of the including provided single crystals

4.2. Microhardness

Following chapter contains the macroscopic hardness results for the single crystalline samples as described in chapter 3.3. The provided hardness values can later be compared to the macroscopic hardness H_0 of the subsequent ISE analysis of the nanoindentation tests.

Cu single crystal

The Cu single crystal was tested with HV 0.1, that corresponds to a load of 100 g. An exemplified indent is shown in Fig. 4.2. The macroscopic hardness amounts 45.2 ± 0.9 HV. The conversion from the Vicker's hardness to the referable SI unit [GPa] results from the multiplication with the factor 0.009807. This leads to a macroscopic hardness of 0.44 ± 0.0087 GPa. According to literature, Cu reveals a macroscopic hardness of 0.40 GPa [65]. This value is slightly smaller than the obtained value and can be referred to different sample preparation. The tested Cu single crystal was mechanically prior to electrolytically polished. Differences in the kind and duration of the metallographic preparation are able to influence the hardness values through strain hardening effects.

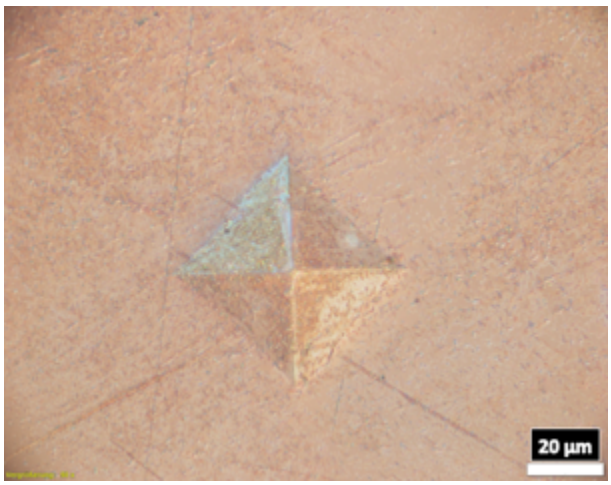

Fig. 4.2: Vickers indent on sx Cu, tested with HV 0.1

Cr single crystal

The Cr single crystal was tested with HV 0.3 (300 g). The related impression is shown in Fig. 4.3. The macroscopic hardness of the tested sx Cr amounts 142.3 ± 2.21 HV. This equates a hardness of 1.40 ± 0.022 GPa. Different to the Cu sample, Cr reveals a higher macroscopic hardness then the hardness described in literature. According to publication data, Cr posseses a macroscopic hardness 0f 1.09 GPa.

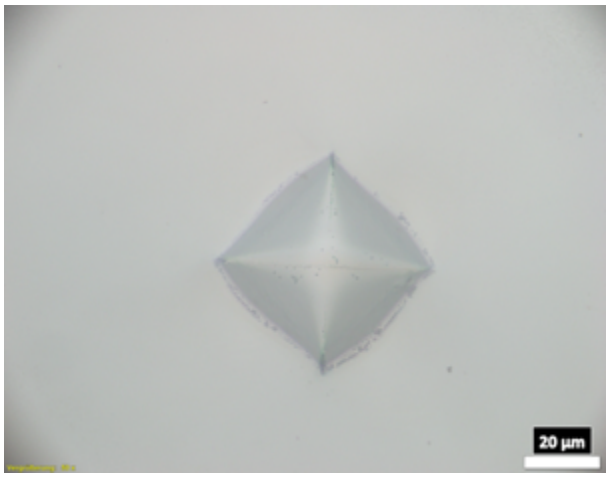

Fig. 4.3: Vickers indent on sx Cr, tested with HV 0.3

W single crystal

The W samples were tested with HV 0.5 (500 g). The resulting hardness values were measured with 343.6 ± 2.90 HV, what corresponds to 3.37 ± 0.03 GPa. Literature reveals a macroscopic hardness of 3.60 GPa [58,61] which is slightly higher than the measured values. The related impression is shown in Fig. 4.4.

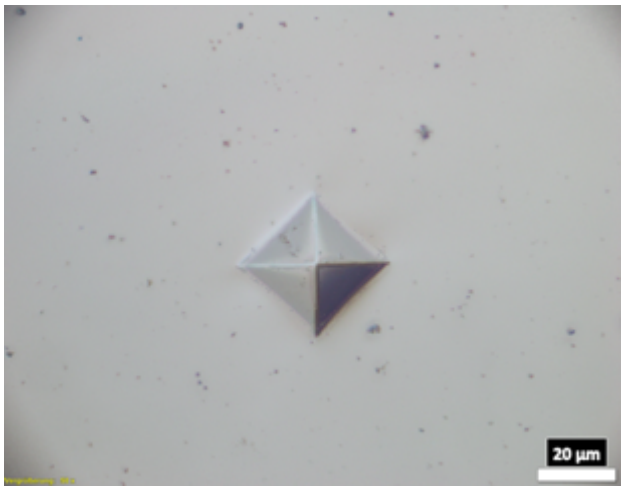

Fig. 4.4: Vickers indent on sx W, tested with HV 0.5

4.3. Nanoindentation

To assess the values for hardness and Young's modulus, the experiments on the single crystals were carried out according to the procedure described in chapter 3.4.3. The indents were performed according an analogical loading-, dwell, and unloading scheme.

Before each indent, a drift analysis was performed. The drift correction for the RT indents was conducted for 40 s, for cryogenic temperatures 120 s. To compensate the high amount of indents and for reasons of qualitative conformability, especially representative numbers including average divergences are presented. Specifically during cryogenic testing, a high amount of outliers values was detected which were not protracted for the calculations of this report. Rejected were indents on which the tip approach failed and thus the program gave back false load displacement curves due to the misdetected surface. Moreover, several curves were excluded which delivered apparently high hardness deviations or abnormalities, which can be retraced to indenting on pores, preparation relics or dirt conglomerations. Furthermore, during cryogenic testing the problem was encountered that after the first indents on the requested temperature, the temperature began to drop. For the sake of competent data coverage, just the first indents of the desired temperature level were taken into account. For all indents a minimum lateral interval was maintained in order to avoid influence of the plastic deformation of the indents amongst each other.

4.3.1. Hardness

This chapter contains the hardness and Young's modulus values for the three different samples at the two temperature levels. The obtained results base on the area function and machine compliance calibration explained in chapter 2.2.2. Due to the fact that the values showed an increase in quality after a set of several indents, the area function was re-calibrated to confirm that the abrasion of the tip could be neglected. A further focus of this chapter is to compare the presented results to accessible literature data and macroscopic hardness measurements. A critical discussion on the errors during measurement including impending challenges will follow in a subsequent chapter.

Cu single crystal

The following Fig 4.5 displays the material response of the different load schemes at room temperature (a) and at -150°C (b). The room temperature curves show an expected increasing slope with rising force during unloading. The upper 30% of the unloading curve is linear and leads to a reasonable fit to obtain the Young's modulus. The testing at

cryogenic temperatures delivers a different material response. The unloading slope is bulged towards the other direction. This phenomenon is well known and results from thermal drift between sample and tip due to slight temperature differences [66]. It is not in accordance with the fitting techniques and leads to a misinterpretation of the obtained values.

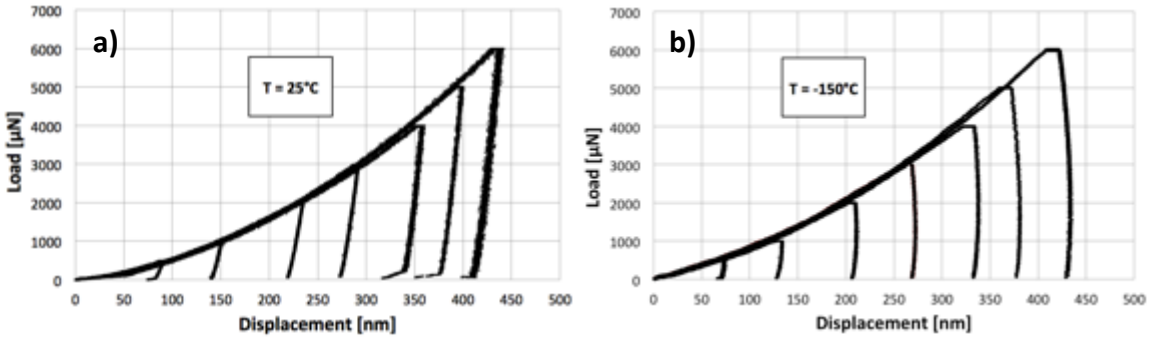

Fig. 4.5: Material response of sx Cu at a) room temperature and b) -150°C at different load levels

The SEM images of the corresponding 3 mN indents are displayed in Fig. 4.6 at a) RT and b) -150°C. Both pictures appear blurred. Probably did an oxide or dirt layer cover the surface in the meantime what in result made a proper imaging of the indents difficult. The other materials did not show this problematic. The CT indent is slightly smaller then the RT indent. The measured imprinted plastic areas A_{pl} are 2.96 µm^2 for RT and 2.60 µm^2 for CT and thus differ with a factor of 1.14. However these values have to be considered with reservation due to the fact that a precise measurement is subject to personal perspective. It is complicated to define the scope of the indent because of the unclear illustration. Regarding the shape of the indents, the dissymmetric profile attracts attention and leads to the assumption that the sample was mounted slightly inclined. This phenomenon pervades throughout the whole investigations. The inclination and possible associated deviations concerning the assessed hardness values will be subject in a subsequent chapter.

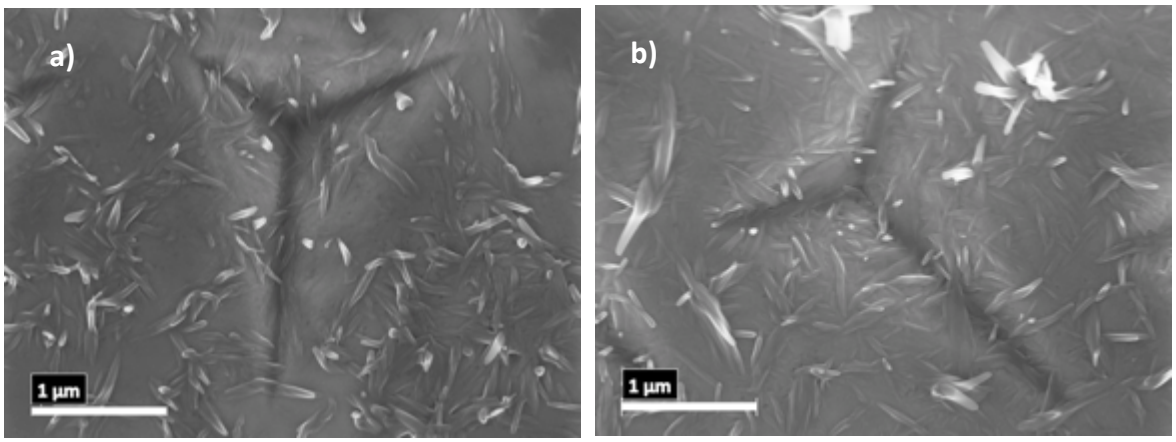

Fig. 4.6: SEM images of 3 mN indents on sx Cu at a) RT and b) -150°

To assess an actual comparison on the room temperature values, the single crystal was tested additionally on a nanoindenter device with integrated continuous stiffness measurement option (CSM), the Keysight G200 located at the ESI in Leoben. These values are displayed in Fig. 4.8 and show an almost perfect accordance amongst each other. The fact that both nanoindentation systems deliver the same values leads to the assumption that machine compliance as well as area function were calibrated correctly. Fig. 4.7 contains as well the values from McElhaney's work. These values are obviously higher than the values obtained by the PI-85 and the G200. The most probable cause of this behavior, which is also described in his work, is that the surface of the annealed single crystal was strain hardened during the metallographic preparation.

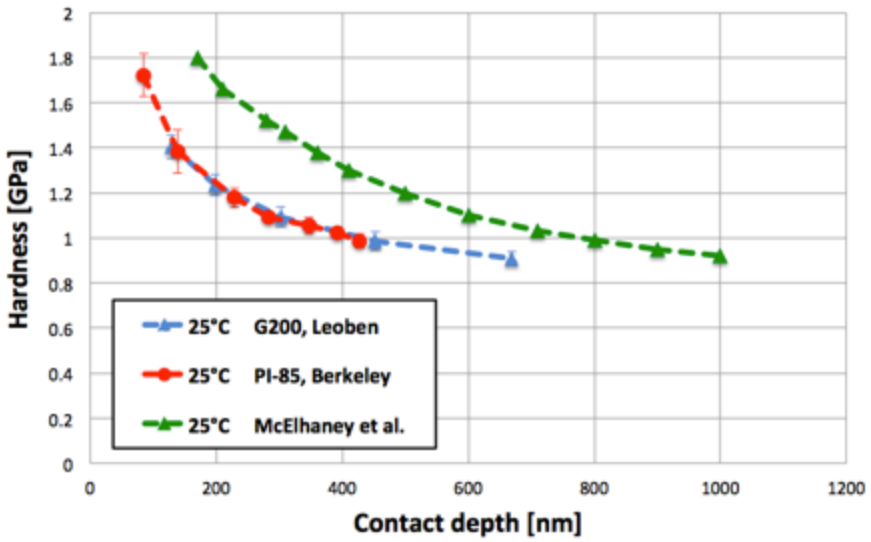

Fig. 4.7: Comparison of room temperature hardness values of sx Cu: PI-85, Berkeley, G200, Leoben and McElhaney's investigations [33].

As shown in Fig. 4.8a, the hardness of sx Cu is decreasing with increasing indentation depth, both for room temperature as well as for -150°C. The room temperature values range from 1.85 ± 0.15 GPa at the lowest force of 0.5 mN and 1.00 ± 0.05 GPa at the highest force of 6 mN. The hardness values at cryogenic temperature range between 2.58 ± 0.55 GPa at 0.5 mN force to 1.17 ± 0.08 GPa at 6 mN force and are thus slightly higher then the room temperature values. However, as shown in the characteristic of the corresponding error bars, the standard deviation for the hardness values at cryogenic temperatures are higher than the deviations at room temperature. Nevertheless, the trend to higher hardness at colder temperature is obvious.

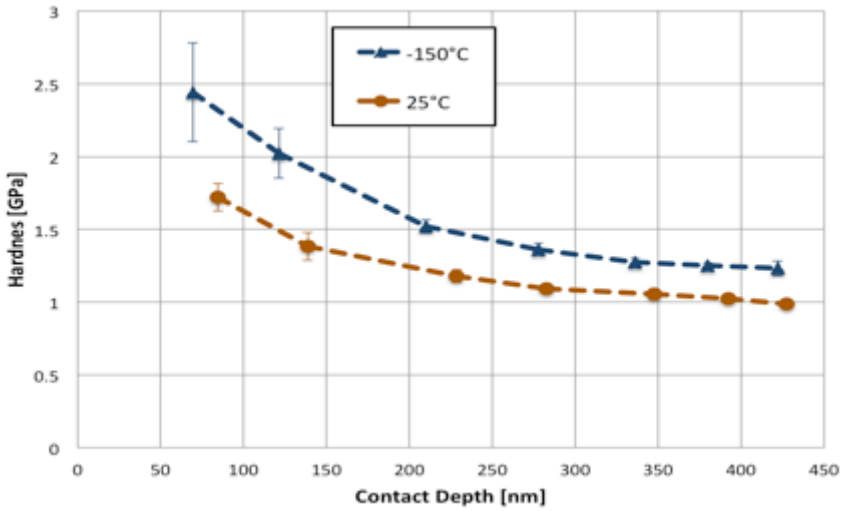

Fig. 4.8: Hardness for the different temperature levels at different contact depth for sx Cu

Cr single crystal

The material response for the indented Chromium single crystal, both for room- as well for cryogenic temperature is displayed in Fig. 4.9. The RT curves express an expected material behavior including the peculiarity of the unloading curve. Different to that, the material behavior at -150°C totally diverges and is quite unusual. The unloading curve is bulged towards the opposite direction. Yet is obvious that the remaining depths are smaller then the corresponding values at RT, although an even smaller value for h_c – supposing that the unloading curve draws back - can be assumed. This phenomenon already was discovered in the CT investigations on sx Cu, yet the expansion of this effect

is quite surprising. It is assumed that enhanced thermal drift is responsible for this occurrence [66]. An attempt to correct these values will follow in a subsequent chapter.

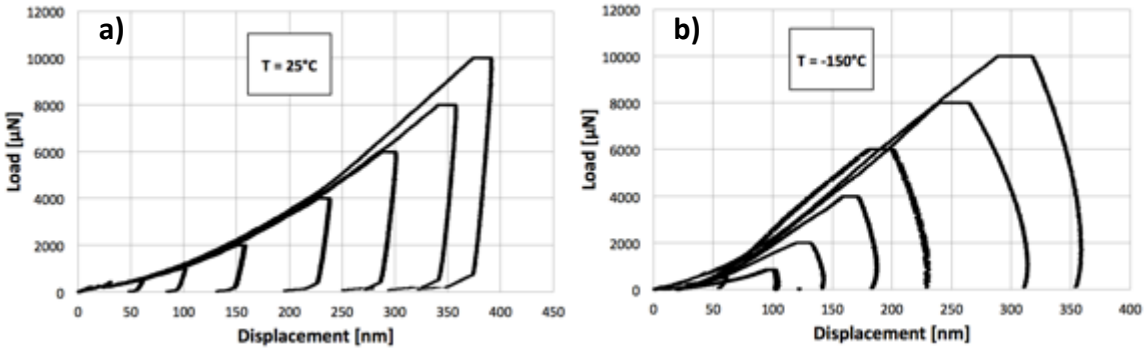

Fig. 4.9: Material response of sx Cr at a) room temperature and b) -150°C at different load levels

Following Fig. 4.10 represents the SEM images of the corresponding indents at a) RT and b) -150°C with a load of 10 mN. The CT indent is obviously smaller then the RT indent. The measured imprinted plastic areas A_{pl} are 3.66 µm^2 for RT and 1.74 µm^2 for CT and thus differ by a factor of 2.1.

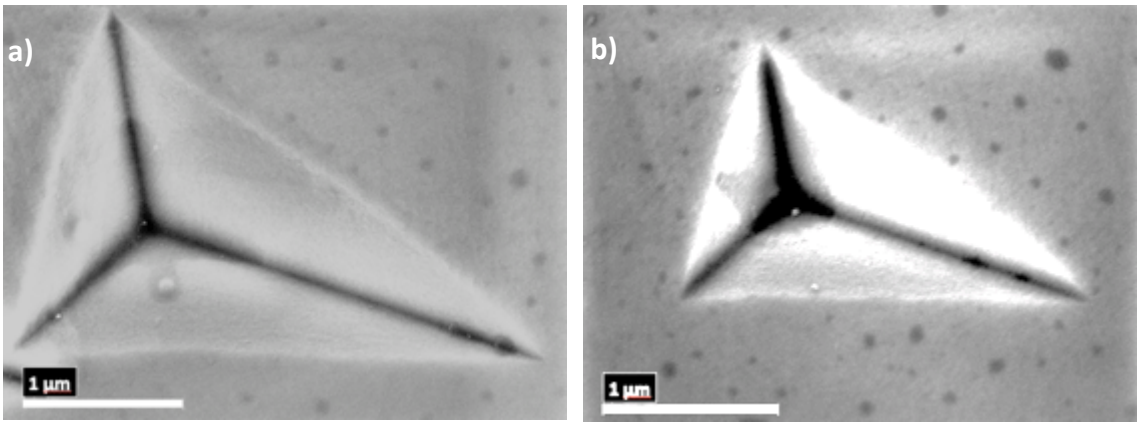

Fig. 4.10: SEM images of 10 mN indents on sx Cr at a) RT and b) -150°

To verify the accuracy of the room temperature values, the Cr single crystal was additionally tested as well on the G200 nanoindentation system at the ESI in Leoben. The comparison of these values, shown in Fig. 4.11 delivers a very good accordance amongst each other. Although the values obtained by the PI-85 in Berkeley posses a higher mean variation, the curves correspond well. This fact leads to the assumption that the

calibration of the area function and machine compliance of the PI-85 was well determined, least at RT.

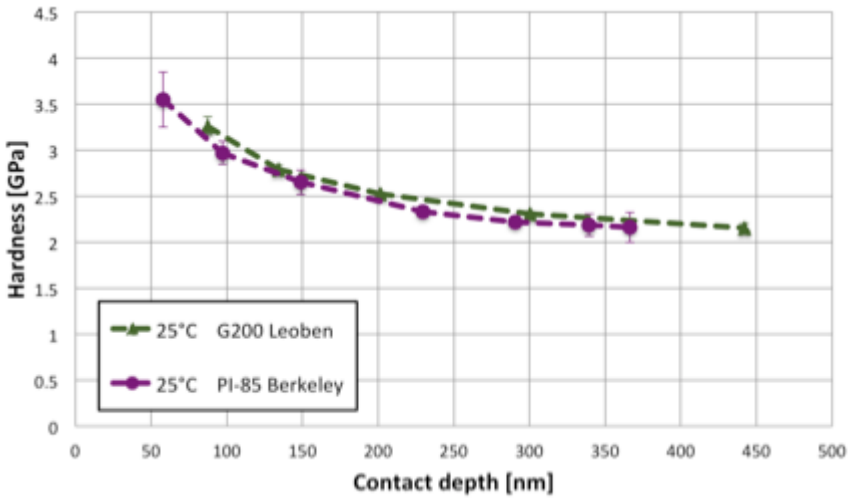

Fig. 4.11: Comparison of room temperature hardness values of sx Cr: PI-85, Berkeley and G200, Leoben

Following Fig. 4.12 represents the hardness values for the different load levels at both, room- and cryogenic temperature. As expected, the hardness values are increasing with decreasing indentation depth, both for room- as well as at cryogenic temperature. At 25°C the hardness increases from 2.16 ± 0.15 GPa at 10 mN load to 3.55 ± 0.11 GPa at 0.5 mN load. The corresponding hardness values at -150°C rise from 3.12 ± 0.27 GPa at 10 mN indentation load to 4.47 ± 1.0 GPa at 0.5 mN load. The hardness at CT is subsequently higher, but obviously rises less recognizably with decreasing indentation depth. However, the deviation at cryogenic temperatures is noticeably higher then at room temperature and in addition rises for smaller indentation depths. Comparing the imprinted areas (Fig. 4.10a and b), a difference between the RT and CT hardness with the factor 2 would be expected. This leads to the assumption that the cryogenic values are influenced by enhanced thermal drift and thus underestimated. The concluding area A_c resulting from the measured contact depth at a load of 10 mN amounts 3.02 ± 0.3 µm^2 and still differ by 0.42% from the optically measured indent.

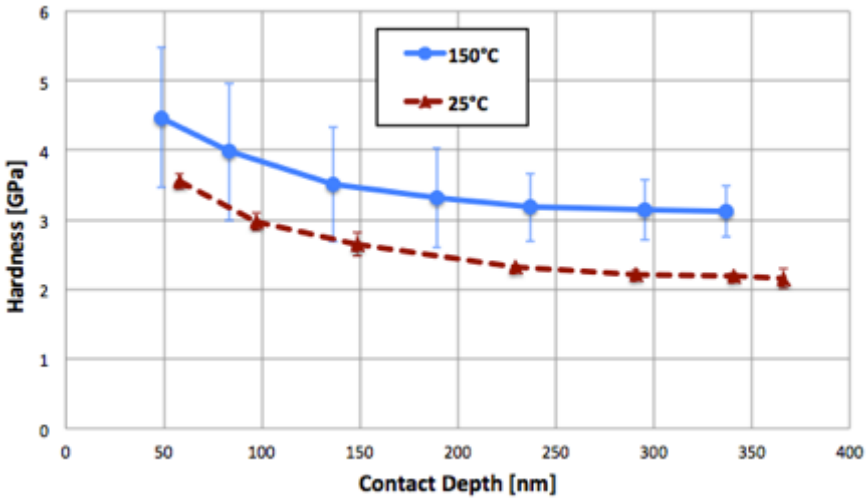

Fig. 4.12: Hardness of sx Cr for the different temperature levels at different contact depth

W single crystal

In following Fig. 4.13, the material response for the sx W samples is displayed, both for (a) room temperature as well as at (b) -150°C. Different to the effects caused by thermal drift experienced with the sx Cu and sx Cr samples, an almost expected material response could be encountered. The upper slope of the unloading curve is linear and leads to representative hardness values for both temperature levels.

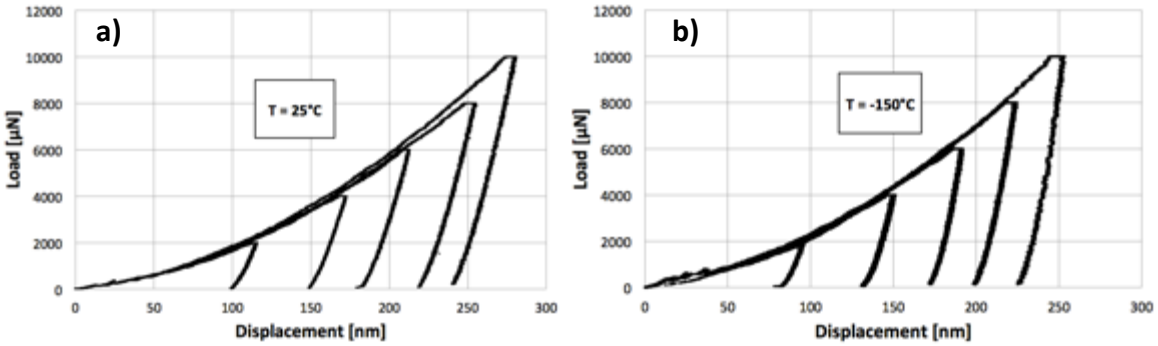

Fig. 4.13: Material response of sx W at a) room temperature and b) -150°C at different load levels

Following Fig. 4.14 show the sx W indents at 10 mN load for a) room temperature and b) -150°C. The measured areas result 1.87 µm^2 for RT and 1.50 µm^2 for CT and thus add up to a factor of 1.25 between the room and cryogenic temperature areas.

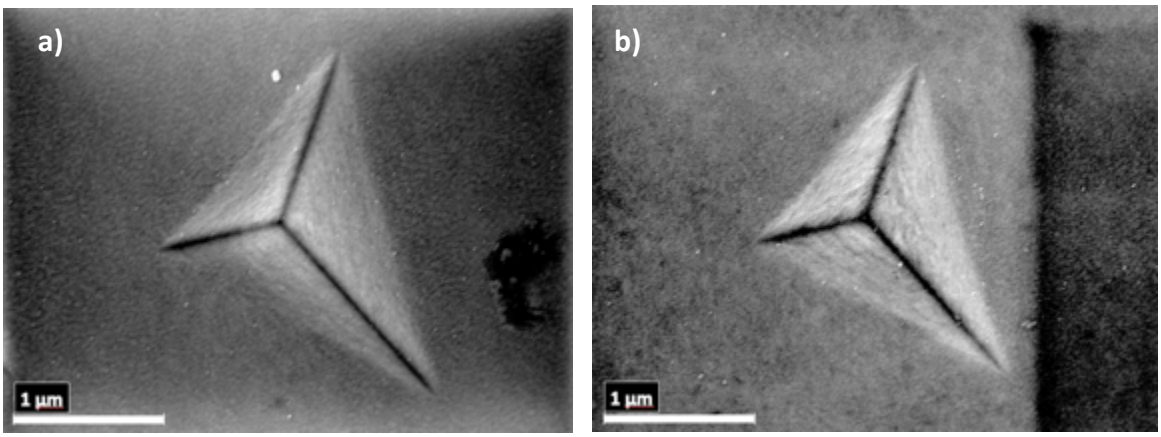

Fig. 4.14: SEM image of 10 mN indents of sx W at a) RT and b) -150°

The comparison of the room temperature values obtained by the PI-85 in Berkeley to the values of nanoindenter in Leoben delivered following Fig. 4.15. The values match well at indentation loads between 4 mN to 10 mN. However, the hardness values obtained by the G200 at Leoben rise significantly below indentation loads of 2.5 mN up to 8.84 ± 0.97 GPa at 0.6 mN load. Although the hardness deviations with almost 1.0 GPa at the smaller loads are very high, the hardness values show an expected increase, different to the values obtained by the PI-85 at Berkeley. Unfortunately representative values from the PI-85 below these load levels couldn't be acquired, but will be part of a discussion in a subsequent chapter.

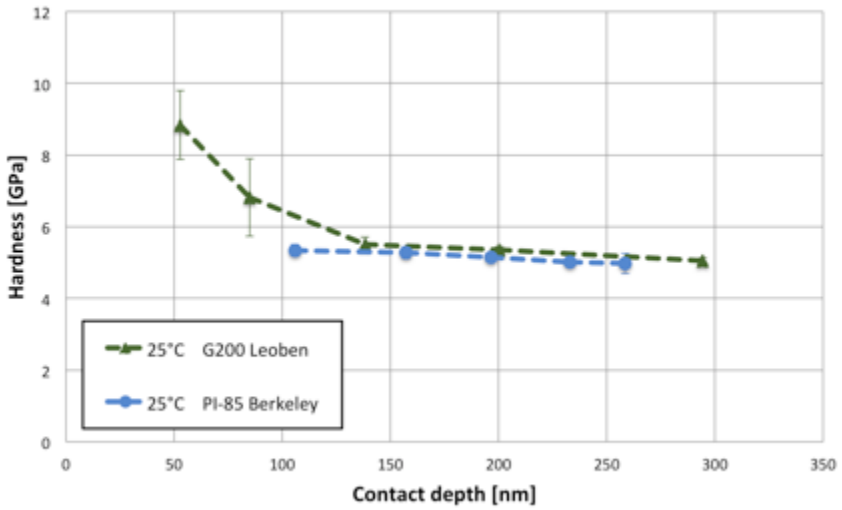

Fig. 4.15: Comparison of room temperature hardness values of sx W: PI-85, Berkeley and G200, Leoben

The hardness values for the different load levels at the different temperatures are displayed in Fig. 4.16. It shows an almost constant hardness at room temperature between the load levels of 2 mN and 10 mN with a slight slope towards the smaller load levels. The hardness values for the cryogenic temperatures are higher than those at room temperature and noticeably rise towards smaller indentation loads. The hardness values for the room temperature experiments rise from 4.97 ± 0.13 GPa at 10 mN to 5.34 ± 0.14 GPa at 2 mN. At cryogenic temperatures, the hardness values range between 6.33 ± 0.29 GPa at 10 mN to 7.73 ± 0.16 GPa. For the room temperature values 10 indents at each load level were observed. For the cryogenic hardness in average 6 indents, but at least 3 indents were taken into account.

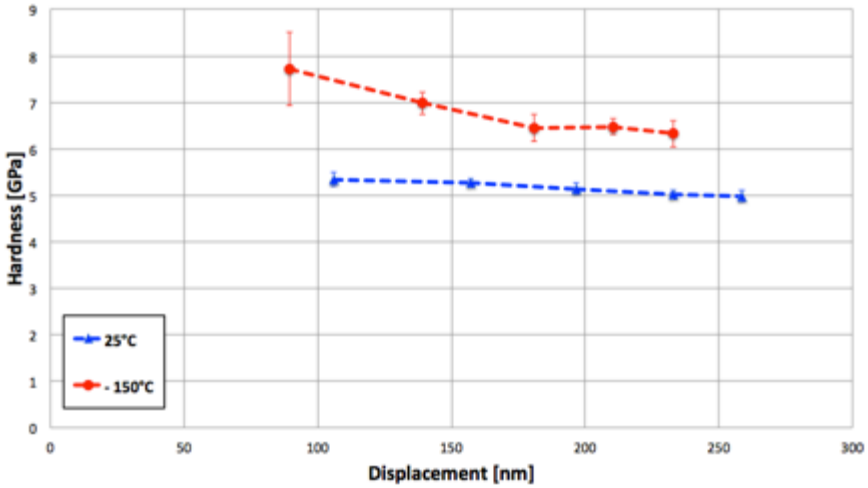

Fig. 4.16: Hardness of sx W for the different temperature levels at different contact depth

4.3.2. Size effect

The calculations on the ISE were carried out according to the scheme described in chapter 2.2.4. H^2/H_0^2 is plotted over the reciprocal values of the corresponding depths *h.* The internal length scale *h** can be enabled directly through the slope of the regression line.

Copper single crystal

The obtained data enabled the following Nix-Gao plot, displayed in Fig 4.17. The fit revealed a macroscopic hardness H_0 of 0.70 GPa at room temperature and a slightly higher value for cryogenic temperature with H_0 = 0.75 GPa. The internal length scale *h**

has been determined to be 422 nm for RT and 690 nm at -150°C. This would lead to the primal assumption that the ISE gains influence with decreasing temperature. The hardness seems to rise stronger at colder temperatures in comparison to ambient temperatures. The comparable data from the different nanoindentation system enabled 0.71 GPa for H_0 and 317 nm for h^*.

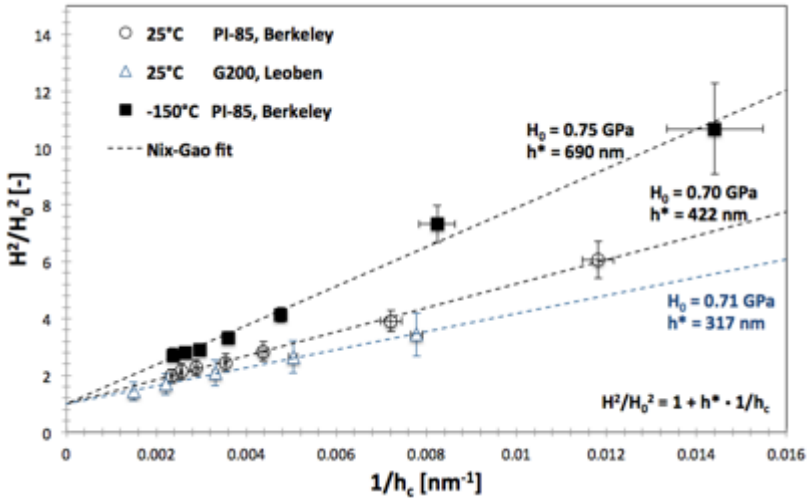

Fig. 4.17: Nix-Gao plot for sx Cu. Comparison of RT and CT, H_0 and h^* values obtained by the PI-85 and the G200

Chromium single crystal

With the hardness data according chapter 4.3.1, the following Nix-Gao plot was constructed. The room temperature data delivered H_0 = 1.78 GPa as macroscopic hardness and H_0 = 2.80 GPa at -150°C. The internal length scale h^* amounts 169 nm, respectively 77 nm at -150°C and is thus in accordance with Maier's assumption that for bcc metals the size effect looses influence below T_c with decreasing temperatures [46]. The additional measurements at the G200 at the ESI in Leoben revealed H_0 = 1.77 GPa and h^* = 206 nm at room temperature and thus quite comparable data. However the values for the internal length scale h^* are below the values from the data of the G200 at Leoben. The applicability of these values respectively their amount is often impeached in literature and will be discussed in a subsequent chapter.

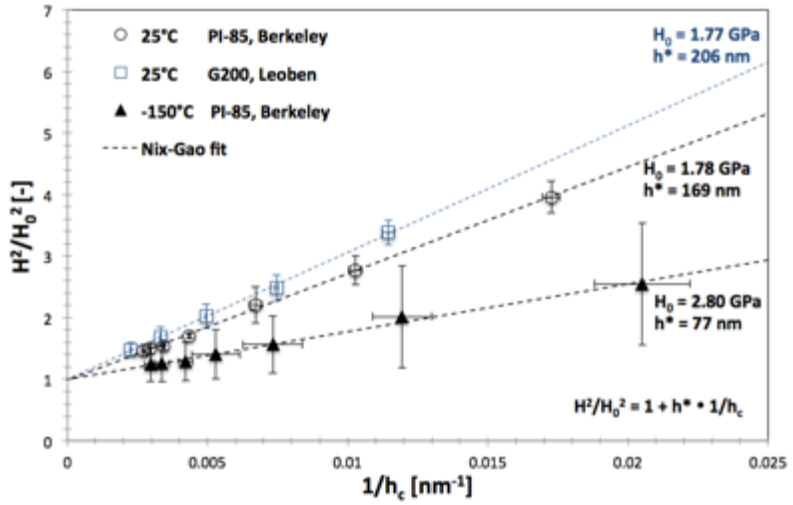

Fig. 4.18: Nix-Gao plot for sx Cr. Comparison of RT and CT, H_0 and h^* values obtained by the PI-85 and the G200

Tungsten single crystal

The Nix-Gao plot for sx W is displayed in Fig. 4.19. The hardness values enabled a macroscopic hardness H_0 at room temperature of 4.75 GPa and at -150°C for 5.24 GPa. The corresponding values for the internal length scale h^* are 30 nm, respectively 105 nm at cryogenic temperature. The additional analysis at the different nanoindenter system delivered H_0 = 4.37 GPa and h^* = 203nm. As mentioned in a previous chapter 4.3.1, further data sets with the PI-85 in Berkeley at both higher and lower loads are missing for a proper analysis of the size effect. An extended load range would compensate the high values of H_0 and enable reasonable values for h^*.

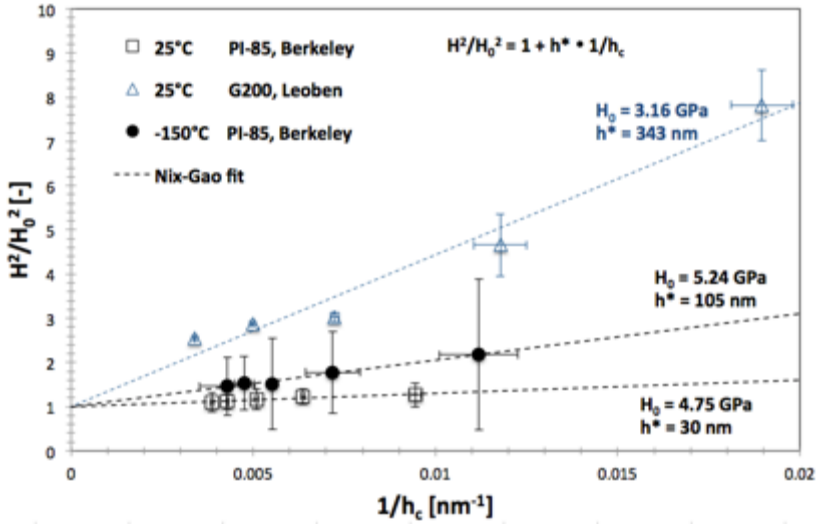

Fig. 4.19: Nix-Gao plot for sx W. Comparison of RT and CT, H_0 and h^* values obtained by the PI-85 and the G200

4.3.3. Pop-Ins

To evaluate the shear stress at the appearing of a pop-in $\tau_{pop\text{-}in}$, the radius of the Berkovich tip, which is assumed to be blunt to some degrees, has to be assessed. This is done in a similar way like the area function is calculated in a so-called fitting routine provided by the HYSITRON® software. Several indents on fused silica below a critical depth, where the tip is assumed to be spherical are analyzed to assess the opening angle of the tip. Due to the fact that a continuous change of the tip radius was encountered as processing the experiments on the ISE and since the tip radius influences the characteristic pop-in load, the tests on the pop-ins were carried out in an additional test series, for which the tip radius was determined up front. To offer a representative analysis with an assumedly constant tip radius, just these indents were taken into account. The tip radius used for these investigations amounted 480nm for the pop-ins at sx Cu and 530 nm for Cr respectively W. The possible change of the tip radius during this set of indents thus was neglected. Fig. 4.20 shows three typical load-displacement curves of sx Cr at RT with apparent pop-in appearing at loads of 640 µN, 1120 µN and 1560 µN.

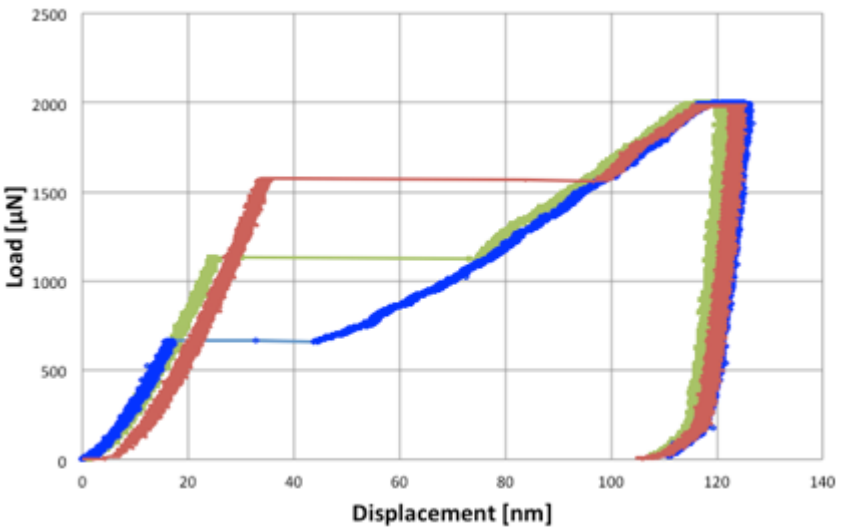

Fig. 4.20: Pop-in events in sx Cr at loads of 640 µN, 1120 µN and 1560 µN

An exemplary array of indents performed for the pop-in analysis is shown in Fig. 4.21 at a) room temperature and b) cryogenic temperature for sx W. These indents were executed with a load of 10 mN, as the RT pop-ins in W typically occurred at 2.56 ± 0.95 mN, the CT pop-ins appeared at 2.92 ± 0.91 mN.

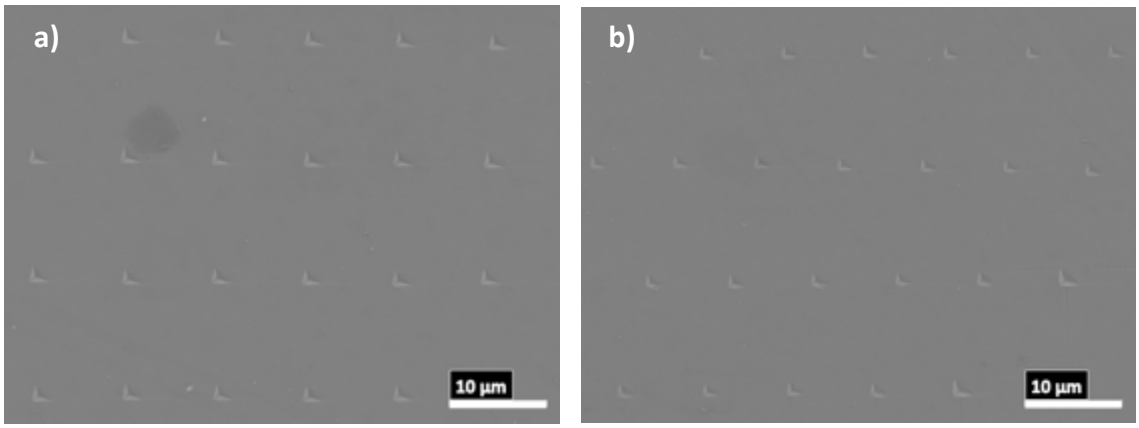

Fig. 4.21: Array of indents performed for the pop-in investigations on sx W at a) RT and b) -150°C

Copper single crystal

For the pop-in investigations on Cu, altogether 93 indents were performed, 53 indents at RT and 40 indents at -150°C. At room temperature in sum 24 pop-ins appeared, resulting a 45% probability. The probability of pop-ins appearing at -150°C was 15%, just 6 pop-ins appeared. Fig. 4.22a shows the cumulative probability of an appearing pop-in at its corresponding load. The probability of a pop-in to appear was higher at room temperature as at cryogenic temperature, Furthermore, pop-ins appeared at -150°C at a higher load than at RT. Cu reveals a theoretical shear stress τ_{th} of 3.64 GPa [67], the average ratio $\tau_{pop\text{-}in}/\tau_{th}$ at RT for a pop-in to appear was 75.3 ± 7.8%. At -150°C the pop-ins appeared at a stress $\tau_{pop\text{-}in}$ of 82.7 ± 13.5% of the theoretical shear stress τ_{th} (Fig. 4.19b).

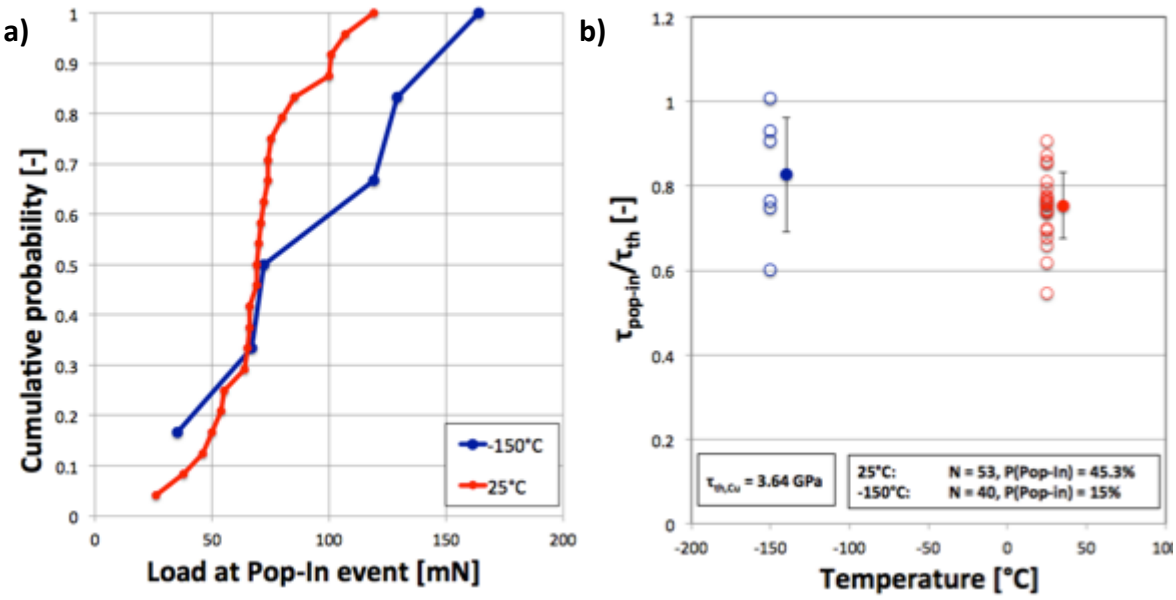

Fig. 4.22: a) Comparison of cumulative probability pop-ins appearing versus corresponding pop-in load at different temperatures of sx Cu b) Theoretical strength versus temperature

Chromium single crystal

For the pop-in investigations on sx Cr altogether 93 indents were analyzed, 37 at room temperature and 46 at -150°C. In Fig. 4.23a the cumulative probability for the pop-ins for sx Cr is shown. The curves are similar, though the cryogenic pop-ins seem to appear at slightly lower loads. The theoretical shear stress for Cr is 18.3 GPa [68]. The relative theoretical shear strength at RT is 11.13 GPa what correlates to a ratio $\tau_{pop\text{-}in}/\tau_{th}$ of 60.8 ± 5.4%. At cryogenic temperature, the relative theoretical shear strength results 11.18 GPa what conforms with a $\tau_{pop\text{-}in}/\tau_{th}$ ratio of 61.14 ± 4.3%.

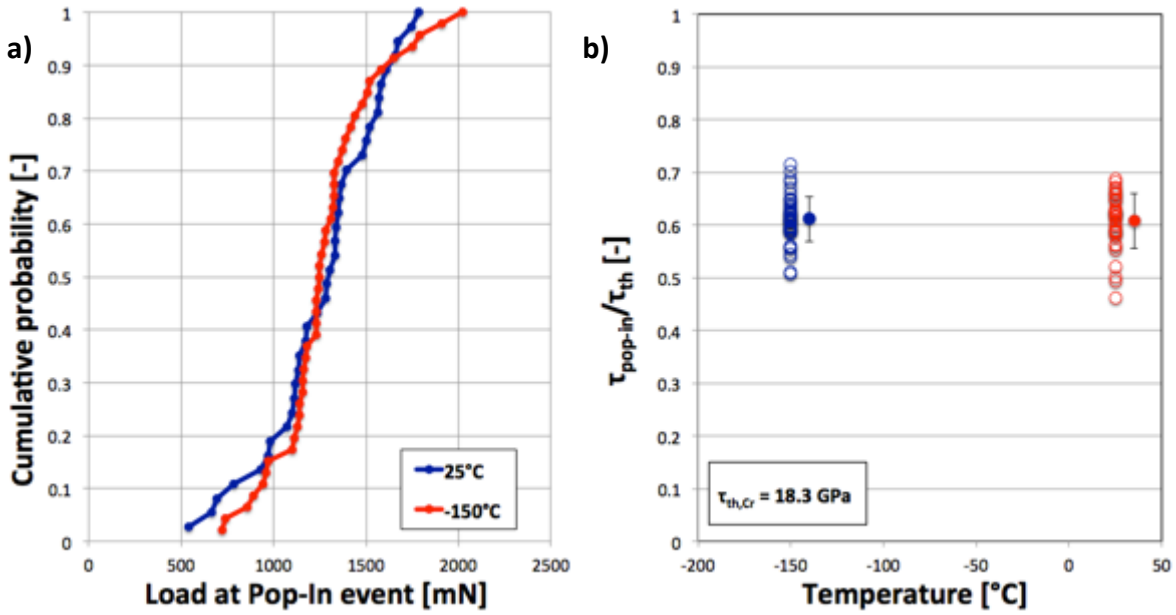

Fig. 4.23: a) Comparison of cumulative probability of pop-ins appearing versus corresponding pop-in load at different temperatures of sx Cr. b) Theoretical strength versus temperature.

Tungsten single crystal

For the W single crystal, the pop-in load at cryogenic temperature is as expected obviously higher than at room temperature as shown in Fig. 4.24a. W possesses theoretical shear strength of 25.6 GPa [62], the relative theoretical shear stress at RT, what was calculated by the pop-in event is 17.27 GPa, respectively 18.18 GPa at -150°C, the correlating $\tau_{pop\text{-}in}/\tau_{th}$ ratios are 67.4 ± 8.9% and 71.0 ± 0.7% at room and cryogenic temperature respectively.

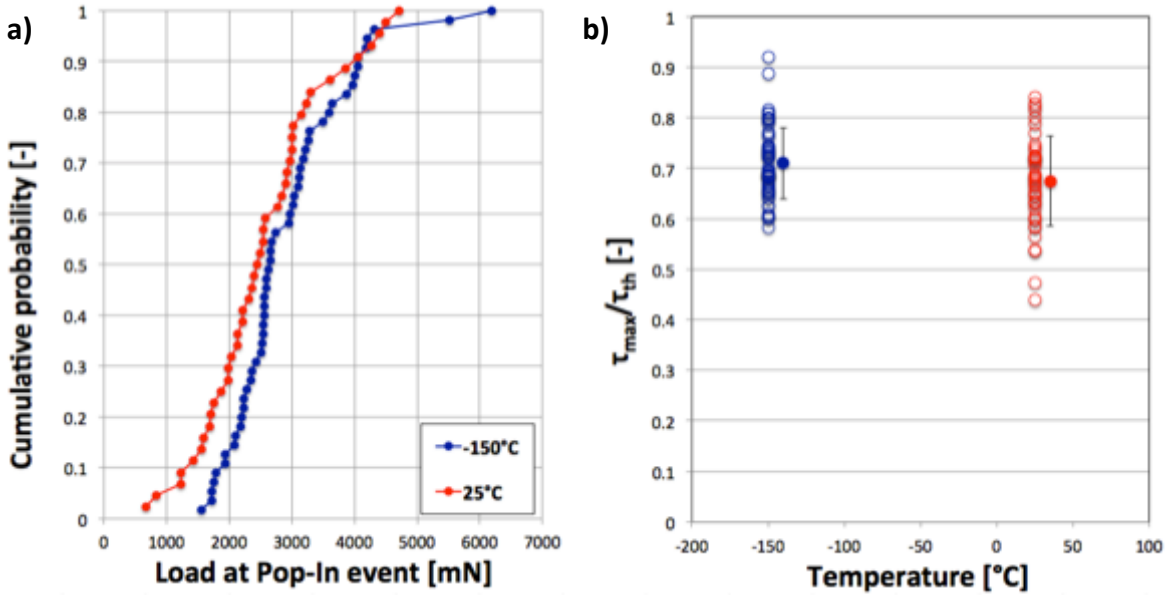

Fig. 4.24: a) Comparison of cumulative probability of pop-ins appearing versus corresponding pop-in load at different temperatures of sx W. b) Theoretical strength versus temperature.

4.4. Tip alteration

The tip and especially its radius do not only influence the area function and so the obtained hardness values, but as well the critical load for an appearing pop-in. As yet explained in chapter 2.2.5, Furthermore, inspected by Wu et al. on Cr single crystals, the pop-in load rises with increasing tip radius [69]. Due to the fact that a continuous change of the tip was encountered as experimenting on the different single crystals, an additional chapter is dedicated to the alteration of the tip.

Fig. 4.25 shows the change of the tip during the different sets of indents. The tip radius was determined through the data sets on fused silica, which were obtained for the area function calculations ahead of each set of experiments.

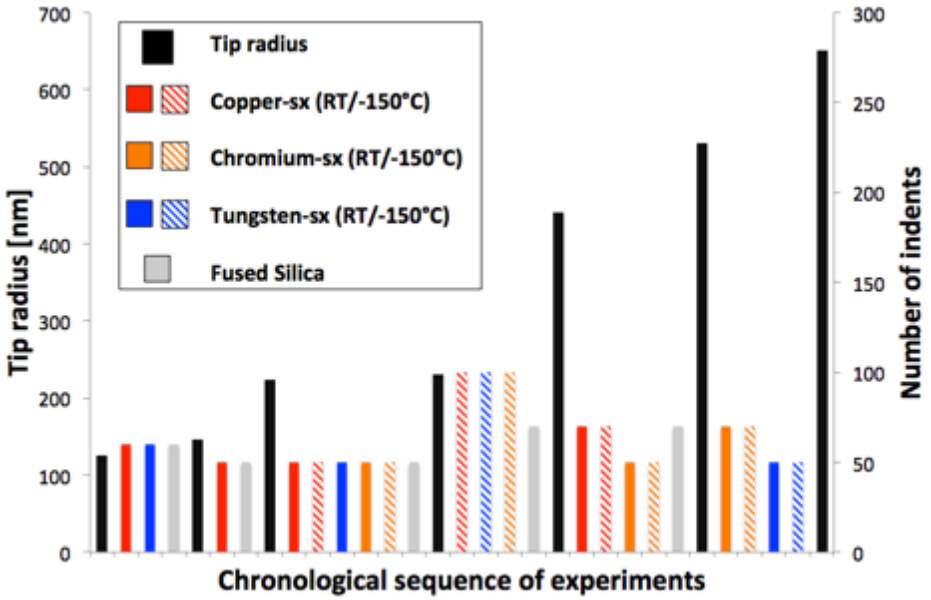

Fig. 4.25: Tip alteration over the scope of experiments

The first experiments were mainly performed at room temperature and did not influence the tip radius. A severe change in the tip radius is encountered after a sequence of cryogenic experiments on all three materials. In a previous test sequence, Cu and Cr were tested at cryogenic temperatures as well but did not show a major effect on the subsequent tip geometry. It seems likely that the cryogenic experiments on W affected the tip radius. The following test sequence did not contain a cryogenic series of W, the tip geometry yet changed but marginal compared to the previous set.

To image the wear of the tip, several indents were inspected via an atomic force microscope, the "Digital Instruments® Dimension 3100" located at the ESI in Leoben. Two indents were examined, both of sx W indented at RT with 10 mN load. The first one from an early batch used for the ISE investigations, the second one from the pop-in investigation at the late stage of my investigations in Berkeley.

Fig. 4.26 demonstrates both the AFM images and the correlating SEM images of those batches. The tip radius increased seemingly, the edges weared off.

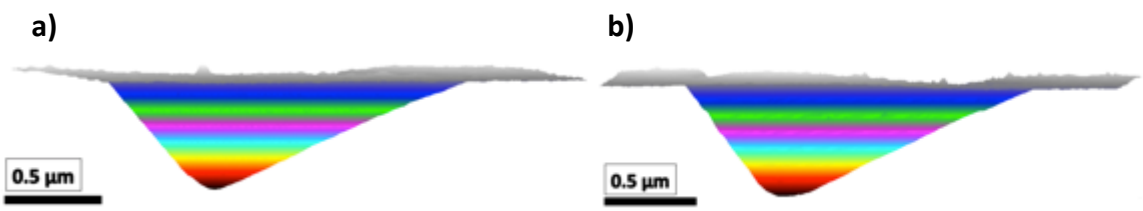

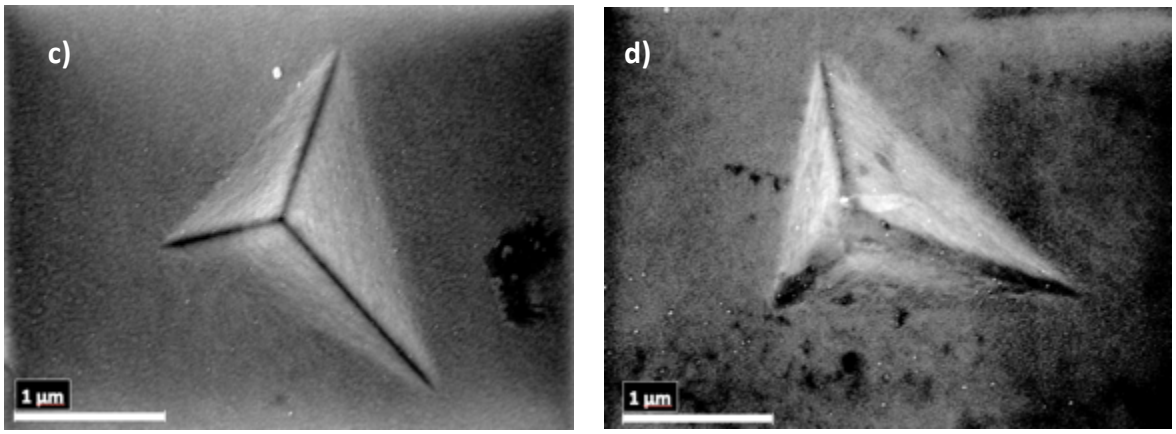

Fig. 4.26: AFM image of indent on sx W with 10 mN, showing the altered tip with tip radii of a) 125 nm and b) 530 nm. c) and d) correlating SEM images

5. Discussion

This chapter is dedicated to evaluate the obtained values and to compare the results to literature data. Furthermore, a critical discussion on the results and the influencing challenges during experimentation will follow.

5.1. Hardness and nanoindentation

5.1.1. Room temperature experiments

Different experiments were conducted to examine the macroscopic hardness for the different single crystals. On the one hand side, the Vickers hardness testing delivered representative values for the hardness on a macroscopic level. On the other side, the Nix-Gao analysis of the size effect provided the macroscopic hardness through the extrapolation of the ISE data. The obtained microhardness values are listed in Table 5.1. It is evident that the hardness values acquired through nanoindentation are higher than the values obtained by conventional hardness testing, in particular Vickers hardness testing. This phenomenon can be justified through the different techniques of analyzing the imprinted area and the different geometrical properties of the used indenters. From the different opening angles between Vickers (136°) and Berkovich (141.9°) follow different values of A_d (real or developed contact area) respectively A_p [18]. As indenting with Vikers, A_p is analyzed. Nanoindentation with a Berkovich indenter reveals A_d. The A_d to A_p ratio amounts 1.0785, resulting in a 7.85% higher hardness value of Berkovich compared to Vickers [25].

Table 5.1: Comparison of RT H_0 values, obtained by different experiments to literature data [12,36,37,58–62,65,70]

H_0 [GPa] / h^* [nm]	sx Cu		sx Cr		sx W	
	Experimental	Literature	Experimental	Literature	Experimental	Literature
Macroscopic hardness	0.44 GPa	0.49 GPa	1.4 GPa	1.09 GPa	3.37 GPa	3.6 GPa
Nanohardness (Nix-Gao fit)	0.70 GPa / 422 nm	0.84 GPa / 472 nm	1.78 GPa / 169 nm	1.6 GPa / 324 nm	4.75 GPa / 30 nm	4.0 GPa / 277 nm

A further reason for the deviations between nanohardness and macroscopic hardness is explained by Rester et al. [39]. According to their investigation it has to be considered between two different deformation mechanisms, dependent on the indentation depth. In large imprints huge orientation changes appear. As deep indentations are always accompanied by an enormous and far-reaching stress field, shallow imprints possess a less extended stress zone, yet long-range dislocation loops to accommodate the shape change of the indenter. Subsequently a bilinear behavior of the size effect appears what accounts for the hardness deviations between macroscopic hardness and nanohardness.

The deviation between the measured macroscopic hardness values and literature data would be explained by a difference in sample preparation. The provided single crystals were electrolytically polished in order to avoid plastic deformation of the material. Kim et al. [36] who improved the previous work of Nix and Gao [7] with a correction of the tip rounding published a macroscopic hardness of 0.84 GPa of sx Cu. This value is 0.14 GPa higher than H_0 investigated in the present work and can be referred to a mechanical sample preparation, what is described in their publication [36]. The deviations of the H_0 values of the other single crystals compared to literature data can as well be retraced to a different sample preparation. As shown, mechanical and electrolytical polishing methods and presumably the duration of both procedures do have an influence on the obtained values. Nevertheless, these minimal deviations have no relevance in this context. The comparison between the obtained nanohardness values and the internal length scale h^* to literature data will be discussed in a subsequent chapter.

5.1.2. Cryogenic experiments

The cryogenic nanoindentation experiments were carried out at a temperature around -150 ± 3°C. As mentioned in a previous chapter, it was a delicate process to set the temperature to the desired level. The temperature was regulated via the intensity of nitrogen stream. After setting the gas flow to a certain level, a waiting period of at least 60 minutes was required until the temperature at the thermocouple attached to the chiller unit settled at a stable level. With decreasing fill level in the liquid nitrogen container, the stream changed and so did the temperature at the testing unit. These temperature variations evoked elevated drift due to the fact that the tip and the sample

reacted different to the temperature change due their different thermal conductivity. The cryogenic advance of the testing device was mainly designed for pillar testing [56], where drift problems play a minor role. The effect of the elevated drift at cryogenic temperatures can be seen in the unloading curve of sx Cu (Fig. 4.7b) or sx Cr (Fig. 4.10b). This leads to a miscalculation of the contact depth h_c (equation 2.6), since the unloading curve defines the stiffness. Yet, even if the cryogenic values have to be considered with reservation, the hardness at CT was higher compared to RT, and this effect was even more pronounced regarding the bcc materials (Table 5.2). This phenomenon can be referred to the elevated Peierl's barrier with decreasing temperatures, through which dislocations are hindered concerning their movement [71]. For sx Cr the temperature independent partition of the shear stress τ^* amounts ~27 MPa. Considering a T_c of sx Cr of 180°C, at RT the thermal fraction τ_t what corresponds to the Peierl's stress is ~41 MPa. This yields to a combined stress τ_{CRSS} of ~68 MPa. At CT τ_{CRSS} for sx Cr is ~690 MPa [13]. The athermal fraction τ^* of W amounts ~34 MPa. At RT it possesses a Peierl's stress of ~57 MPa what leads to a combined stress of 91 MPa. At CT τ_{CRSS} amounts ~924 MPa. These values were calculated through Wang and Marcinkovski's [13,72] research containing a formulation of the Peierl's stress and its temperature dependence at low temperatures. Thus, they represent just an approximation and no confirmed values. Factors such as the Debye temperature, which according to Wang's [72] research do have an influence too, were not considered [13,18].

Furthermore, the hardness of sx Cr rises obviously stronger than that of sx W. The hardness increase amounts to 58% for sx Cr and 10% for sx W, respectively 24%, if the hardness values obtained by the G200 are compared to literature data from Lee et al.'s investigations on sx W [73]. The relative testing temperature T/T_c of W at RT is with a value of 0.37 very small compared to that of Cr with 0.66 [14,16]. Decreasing the temperature to -150°C consequently has a more pronounced effect for Cr concerning its relative testing temperature, which is reduced to 0.27 compared to W, for which T/T_c at CT amounts to 0.154. The smaller T/T_c becomes, the more the Peierl's barrier increases including rising tensile strength and hardness.

Table 5.2: Comparison of RT and CT H_0 values

H_0 [GPa]	sx Cu	sx Cr	sx W
RT	0.70 GPa	1.77 GPa	4.75 GPa, (3.16 GPa)[1]
CT	0.75 GPa	2.80 GPa	5.24 GPa, (3.93 GPa)[2]

H_0 obtained by: [1] G200, Leoben [2] Lee et al. [73]

5.2. Size effect

The investigations on the size effect delivered in general reliable results and confirmed our initial hypothesis. Regarding Cu sx as representative for a fcc metal, the size effect is more pronounced at colder temperature, h^* increases with decreasing temperature. This effect was discovered by Franke et al. [45] on experiments above RT, as well as by Lee et al. [73] on experiments below RT to cryogenic temperatures. Fig. 5.1 demonstrates this increasing size effect with decreasing temperatures on basis of Franke's investigations [45] and the obtained values of the cryogenic experiments in Berkeley.

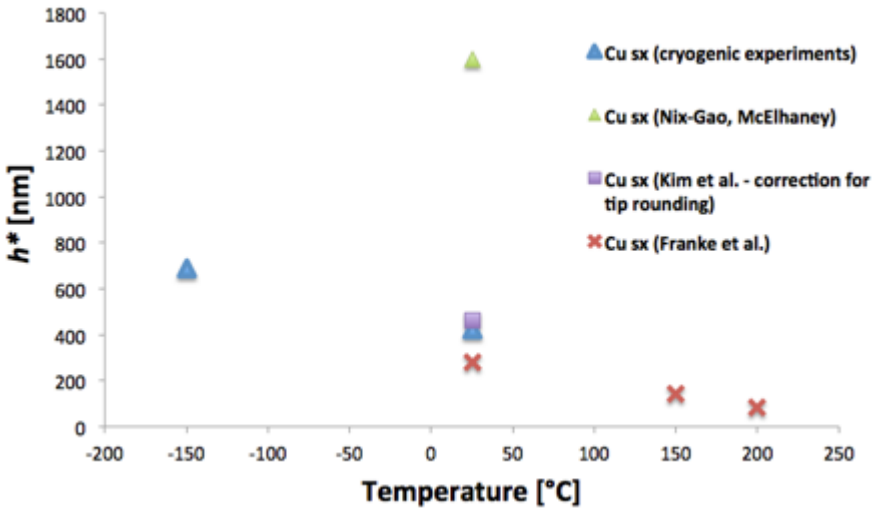

Fig. 5.1: Temperature dependence of the size effect, comparison of Franke's investigations [45] and cryogenic experiments on sx Cu

Franke et al. [45] stated two origins for this effect. On the one hand side the elevating temperature decreases lattice friction and subsequently increases the mobility of dislocations. This correlates to the increasing local density of GNDs in the immediate surrounding of the imprint and successively to the decreasing value for the internal length scale *h**. The second explanation would arise from the increase of SSD with mild temperature increase through thermal activation. Lee et al. [73] presented that yet *h** is both temperature and material dependent, but in general correlates with the intrinsic lattice resistance. Accordingly, materials with high intrinsic RT lattice resistance such as W display an intensification of this characteristic with decreasing temperature, which reveals itself in an increase of the size effect.

The investigations on the W single crystal delivered reliable values, both for room temperature as well as at -150°C due to the fact that these experiments obviously were not affected by accentuated thermal drift. Yet, as mentioned in chapter 4.2 for the hardness analysis of sx W a wider range of applicable forces were necessary. Due to the immense hardness of W, the resulting indentation depths were very small and the observed range was kept in a limit. It can be assumed that the considered region was already in the middle stage of the increasing slope of the size effect curve. Oliver and Pharr investigated a hardness increase of sx W from 3.5 – 5.8 GPa at displacements between 50 and 1000 nm [74]. The measurements with the PI-85 delivered hardness values between 5.0 and 5.3 GPa at depths between 100 260 nm. The lack of data above the maximum applicable loads prohibits a proper analysis of the size effect and its accompanying values H_0 and *h*.* Any interpretation of the obtained data would be very speculative without an extended view on the hardness development over a broader range of indentation depths.

Different to the temperature dependence of the ISE of sx Cu, the size effect of sx Cr decreases with decreasing temperatures. Fig. 5.2 displays a comparison of the *h** values of sx Cr obtained by the PI-85 to the investigations of Maier et al. [46]. Maier reported a decreasing of the internal length scale with increasing temperatures above T_c[1]. This behavior correlates to that of fcc metals as described by Franke et al. [45]. Below T_c, *h** decreases with reduced temperatures. Lee et al. investigated the same trend of bcc materials during cryogenic nanoindentation of sx Nb and tried to explain that effect with

the high lattice resistance of bcc metals with increasing *T,* which is also associated with a low cross slip probability [73].

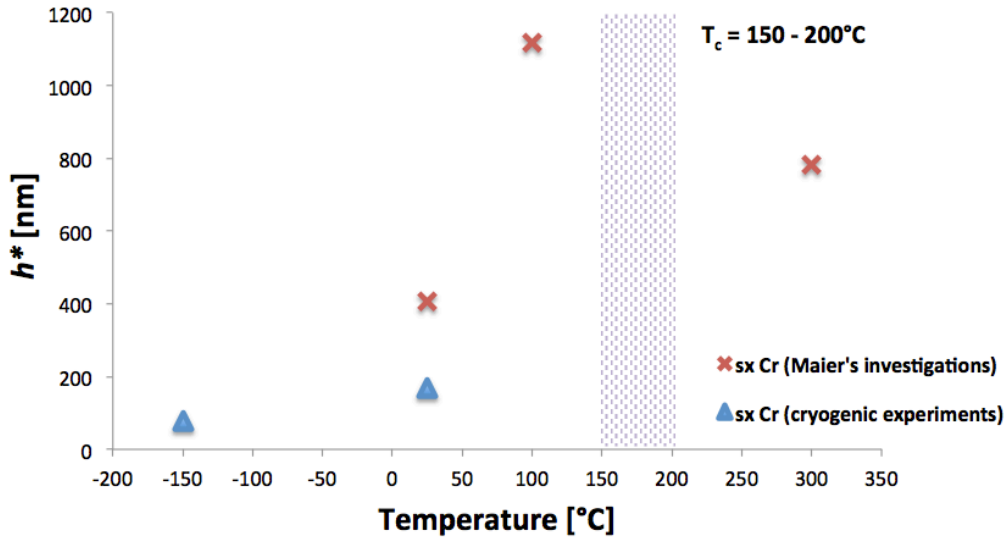

Fig. 5.2: Temperature dependence of the size effect. Comparison of Maier's investigations and cryogenic experiments on sx Cr [46]

[1] As mentioned in chapter 2.1, the critical temperature is rather a temperature range than a defined temperature point.

5.3. Pop-ins

Examinations on the pop-in events constitute a rewarding task due its uncomplicated execution. These kinds of experiments are diminutively predisposed by thermal drift problems. The unloading curve has no relevance for these investigations. Furthermore, the area function has no significance as soon the tip rounding is identified. Nevertheless, as demonstrated in chapter 4.4, the alteration of the tip did play a major role during the investigations. It is likely that the tip radius even during testing did alter. This assumption would explain the comparable decreasing pop-in load on the cryogenic pop-in investigations on sx Cr. With increasing tip-radius, the pop-in load increases as well. Fig. 5.3 demonstrates the cumulative probability of pop-ins with decreasing tip radius. A 50% reduction of the tip radius would increase the pop-in load by 200%.

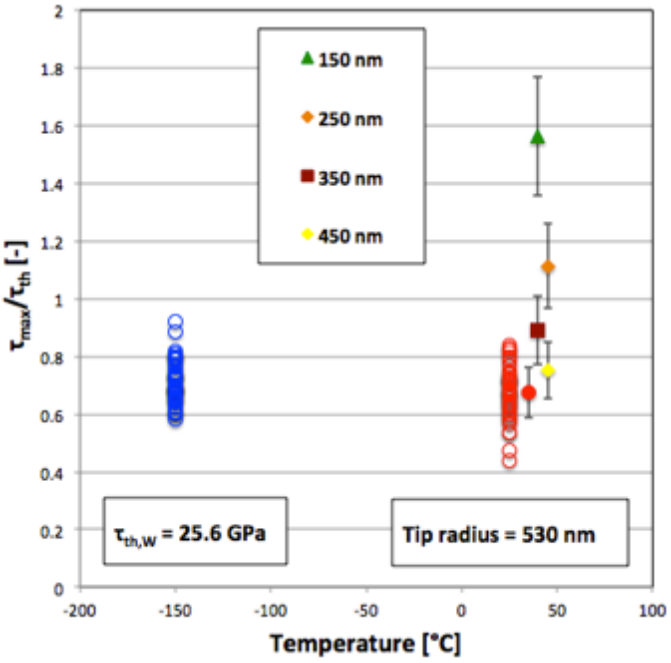

Fig. 5.3: Cumulative probability of pop-ins of sx W, comparison of RT and CT, different $\tau_{pop\text{-}in}/\tau_{th}$ ratios with decreasing tip radius

The high radius of 530 nm approaches the tip geometry of spherical indenters, which usually have radii of >1 µm [18]. Phani et al. [75] investigated the tip radius dependence of spherical indenters on the pop-in event. They showed that increasing tip radii of 580 nm and higher again decrease the maximum shear stress at the pop-in. Yet with a tip radius of around 500 nm the pop-in appears at a maximum shear stress what corresponds to the theoretical shear stress of the material. The pop-ins of the investigated single crystals appeared at stresses minimal smaller than τ_{th}. In the present case, at RT the $\tau_{pop\text{-}in}$ /τ_{th} ratios amount to 75.3 ± 7.8% for sx Cu, 60.8 ± 5.4% for sx Cr and 67.4 ± 8.9% for sx W respectively. As described in a previous chapter, τ_{max} can be assumed as the theoretical shear strength of the material in the case of a homogenous nucleation of dislocation of a dislocation free material [50]. The maximum shear stress required for the incipient plasticity was observed to be within 1/6 to 1/7 of the shear modulus and thus in good accordance with τ_{th}. The $\tau_{pop\text{-}in}$ /τ_{th} ratios were diminutively higher at CT then at RT and amounted to 82.7 ± 13.5% for sx Cu, 61.14 ± 4.3% for sx Cr and 71.0 ± 0.7% for sx W. It is obvious that decreasing the ambient temperature will lead to an increase of the critical load what is necessary to trigger the pop-in. This temperature dependence of the pop-in event has been reported in several materials such as sx Cr above RT [68] and sx Pt [76].

5.4. Critical discussion on experimental challenges

Oblique sample mounting through equipment adaption

Through the adaption of the PI-85 to a cryogenic testing unit, the equipment was advanced as shown in Fig. 3.2 with an additional copper plate to enable the cooling of the sample. This plate extended the original size of the indenter and lead to an overlapping of the transducer stage. Below the transducer stage were four props located to ensure a plane position of the stage. Due to the adaption through the additional plate, two of these props protruded from the application what lead to a diminutive oblique mounting of the stage and thus the sample. Laurent-Brocq et al. [77] investigated the influence of roughness and tilt on nanoindentation measurement in a quantitative model. They showed the deviations between the hardness of non-tilt and tilt (2°, respectively 5°) stainless steel probes. With the help of a geometric model (Fig. 5.3) they approximated the printed area of an inclined indent and offered a correction of the obtained values dependent on the tilt angle. Nevertheless, this correction assumes that the inclination is known. In the specific case of the present thesis the deviation was not known, yet with the help of SEM images this geometric model was used to calculate the tilt according to equation 5.1:

$$\tan\theta = \frac{h \cdot 2 \cdot \sqrt{3}}{B} - \frac{1}{\tan\alpha} \tag{5.1}$$

where ϑ is the tilt angle, h is the contact depth of the correlating indent, B is the shortest side of the half symmetric imprint (Fig.5.4a) and α (65.27°) is the characteristic angle of the tip [25].

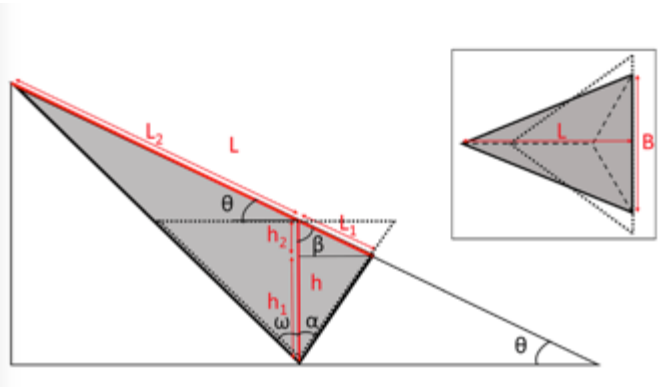

Fig. 5.3: Scheme of a print obtained by nanoindentation on a tilted surface according to Laurent-Brocq. Cross view and top-view (right corner) [77]

The dimensions were analyzed with the image processing program "*ImageJ®*". With *h* = 366 nm and *B* = 2300 nm, the inclination amounts 5.20°. Notably, this geometrical model is only applicable if the indent is axis-symmetric and the contact depth is known. To asses the actual tilt without *h* and for non-symmetric indents, the 3D CAD design software "*SolidWorks®*" was used to construct a model by witch the angle can be identified.

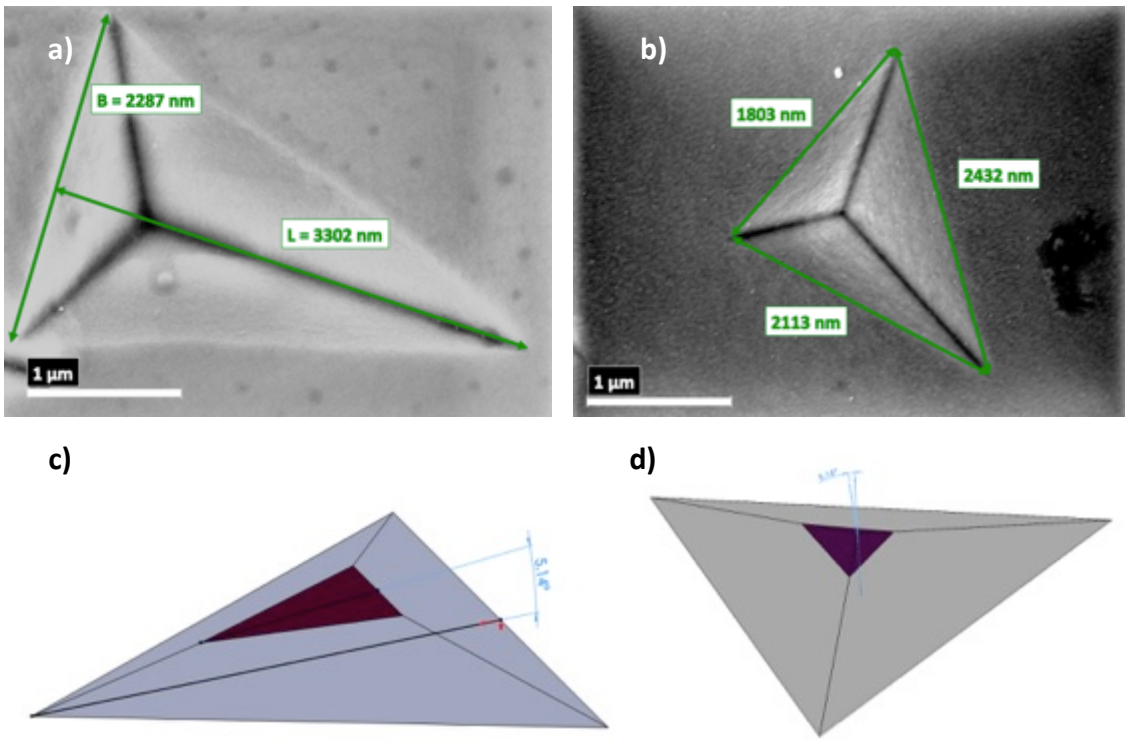

Fig. 5.4: SEM images of inclined indents of a) sx Cr 10 mN at RT and b) sx W 10 mN at RT. Geometrical dimensions analyzed with an image processing program. c + d) Correlating CAD model showing the identified angles.

The constructed model delivered an angle of 5.14° for sx Cr, respectively 5.16° for sx W and thus identical inclinations as with the geometrical analysis by the model of Laurent-Brocq [77]. Due to the fact that the hardness values of both indents are in accordance with the RT values obtained with the G200 at the ESI Leoben, where no inclination was detected, it can be assumed that even the calibration on fused silica was performed on a tilted sample. The angle and the associated deviation subsequently was adapted and corrected. Accordingly, the obtained values in the present thesis were not further corrected regarding tilt mounting. It is well known that the crystallographic orientation obtains a significant influence on the hardness of single crystals [78]. Nevertheless, it can

be assumed the relatively small inclination did not influence the testing concerning activating a different crystallographic orientation.

Accentuated drift and consequences on obtained values

The temperature deviation between sample and tip caused augmented drift and thus displeasing problems during testing [66]. These drift issues, which could not be eliminated, influenced the obtained results. An attempt was made to correct a selected load displacement curve of an experiment at cryogenic temperature. The original curve (Fig. 5.5 – green curve) was adapted with a manual input of random parameters for machine compliance and drift until the unloading slope of the curve showed an expected shape (red curve). The original compliance amounted to 1.81 nm/mN and was corrected to 5 nm/mN. The testing program calculated the drift to be -2.48 nm/s. To this value 3 nm/s were added to construct the green curve in Fig. 5.5.

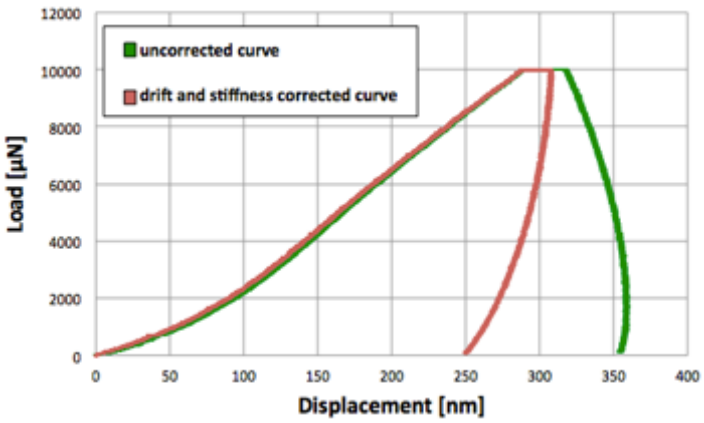

Fig. 5.5: Attempt to correct an unloading curve of sx Cr at CT with changing parameters of drift and compliance

The hardness based on this corrected curve was calculated to be 3.7 GPa and differs to the original value of 3.12 GPa by 19%. It has to be considered that this attempt is not based on real values but approached by changing the parameters randomly. Nevertheless, it is obvious that thermal drift causes high deviations and the affected values have to be considered with reservation.

6. Conclusion

Three different single crystalline materials, namely Cu, Cr and W were examined at RT and at -150°C with a PI-85 nanoindentation device to investigate the ISE and its temperature dependence. Furthermore, the probability of pop-ins was analyzed at both temperatures. The research on the size effect at RT delivered reliable values, which were in good accordance both to literature and to reference tests on a second nanoindenter system. The examinations at CT were highly affected by thermal drift. Subsequently, the obtained values have to be regarded with reservation. Yet, it was shown on sx Cu that fcc metals reveal an increasing size effect with decreasing temperature, which is in agreement with Franke's investigations on fcc metals at elevated temperatures [45]. Contrary, the size effect of bcc metals, demonstrated on sx Cr, seems to decrease with reduced temperatures, as it depends on the critical temperature as shown by Maier et al. at RT [46,70]. For the examinations on sx W, an extended load range would have been necessary to a better insight on the ISE over a broader field of indentation depths. Moreover, we find that the critical pop-in load rises with decreasing temperature. Furthermore, SEM investigations showed an inclined sample mounting caused by the adaption of the equipment to perform tests at cryogenic temperatures. It is determined that the calibration on fused silica already corrected the inclination of 5° in the hardness analysis.

The research on the cryogenic behavior of the ISE constitutes a high potential concerning investigation of material behavior at non-ambient temperatures and temperature dependent material performance. Yet, challenges due to enhanced thermal drift complicated the examinations. To confirm the obtained values, a continuation of the cryogenic investigations with a focus on eliminating the issues concerning thermal drift would be necessary.

7. Literature

[1] R. P. Feynman, “There’s plenty of room at the bottom,” *Engineering and science*, vol. 23, no. 5, pp. 22–36, 1960.

[2] G. Binnig, C. F. Quate, and C. Gerber, “Atomic force microscope,” *Physical review letters*, vol. 56, no. 9, p. 930, 1986.

[3] T. Suzuki, S. Takeuchi, and H. Yoshinaga, *Dislocation Dynamics and Plasticity*. Springer Berlin Heidelberg, 2013.

[4] W. C. Oliver and G. M. Pharr, “An improved technique for determining hardness and elastic modulus using load and displacement sensing indentation experiments,” *Journal of Materials Research*, vol. 7, no. 06, pp. 1564–1583, 1992.

[5] N. A. Fleck, G. M. Muller, M. F. Ashby, and J. W. Hutchinson, “Strain gradient plasticity: Theory and experiment,” *Acta Metallurgica et Materialia*, vol. 42, no. 2, pp. 475 – 487, 1994.

[6] N. Fleck and J. Hutchinson, “A phenomenological theory for strain gradient effects in plasticity,” *Journal of the Mechanics and Physics of Solids*, vol. 41, no. 12, pp. 1825–1857, 1993.

[7] W. D. Nix and H. Gao, “Indentation Size Effects in Crystalline Materials: A Law for Strain Gradient Plasticity.” Journal of the Mechanics and Physics of Solids, 1998.

[8] G. Gottstein, *Physical Foundations of Materials Science*. Springer, 2001.

[9] F. J. Humphreys, *Recrystallization and Related Annealing Phenomena*. Elsevier Science, 2012.

[10] A. Seeger, “The temperature dependence of the critical shear stress and of work-hardening of metal crystals,” *The London, Edinburgh, and Dublin Philosophical Magazine and Journal of Science*, vol. 45, no. 366, pp. 771–773, 1954.

[11] R. Gröger and V. Vitek, “Temperature and strain rate dependent flow criterion for bcc transition metals based on atomistic analysis of dislocation glide,” *International Journal of Materials Research*, vol. 100, no. 3, pp. 315–321, 2009.

[12] V. Maier, A. Hohenwarter, R. Pippan, and D. Kiener, “Thermally activated deformation processes in body-centered cubic Cr – How microstructure influences strain-rate sensitivity,” *Scripta Materialia*, vol. 106, pp. 42–45, Sep. 2015.

[13] M. J. Marcinkowski and H. A. Lipsitt, “The plastic deformation of chromium at low temperatures,” *Acta Metallurgica*, vol. 10, no. 2, pp. 95 – 111, 1962.

[14] U. Holzwarth and H. Stamm, “Mechanical and thermomechanical properties of commercially pure chromium and chromium alloys,” *Journal of Nuclear Materials*, vol. 300, no. 2, pp. 161–177, 2002.

[15] B. A. Wilcox, N. D. Veigel, and A. H. Clauer, “Ductile-brittle transition of thoriated chromium,” *Metallurgical Transactions*, vol. 3, no. 1, pp. 273–283, 1972.

[16] D. Brunner and V. Glebovsky, “The plastic properties of high-purity W single crystals,” *Materials Letters*, vol. 42, no. 5, pp. 290–296, Feb. 2000.

[17] A. S. Schneider, D. Kaufmann, B. G. Clark, C. P. Frick, P. A. Gruber, R. Mönig, O. Kraft, and E. Arzt, “Correlation between Critical Temperature and Strength of Small-Scale bcc Pillars,” *Physical Review Letters*, vol. 103, no. 10, Aug. 2009.

[18] A. C. Fischer-Cripps, “Nanoindentation.” Springer Science+Business Media New York, 2002.

[19] Q. Wei, S. Cheng, K. . Ramesh, and E. Ma, “Effect of nanocrystalline and ultrafine grain sizes on the strain rate sensitivity and activation volume: fcc versus bcc metals,”

Materials Science and Engineering: A, vol. 381, no. 1–2, pp. 71–79, Sep. 2004.
[20] K. Durst and M. Goken, “Nanoindentierung-eine Sonde fur die lokalen mechanischen Eigenschaften,” *Sonderbande der praktischen Metallographie*, vol. 36, p. 319, 2004.
[21] B. N. Lucas and W. C. Oliver, “Time Dependent Indentation Testing At Non-Ambient Temperatures Utilizing the High Temperature Mechanical Properties Microprobe,” in *Symposium B2 – Thin Films: Stresses and Mechanical Properties V*, 1994, vol. 356.
[22] HYSITRON, “SEM PicoIndenter User Manual, Revision 9.3.0913.” 2012.
[23] Verena Maier, “Verformungsverhalten von ultrafeinkörnigen Metallen untersucht mittels neu entwickelter Nanoindentierungsmethoden,” 2013.
[24] G. M. Pharr, W. C. Oliver, and F. R. Brotzen, “On the generality of the relationship among contact stiffness, contact area, and elastic modulus during indentation,” *Journal of materials research*, vol. 7, no. 03, pp. 613–617, 1992.
[25] H. Czichos, T. Saito, and L. R. Smith, *Springer Handbook of Materials Measurement Methods*. Springer, 2006.
[26] M. J. Schulz, A. D. Kelkar, and M. J. Sundaresan, *Nanoengineering of Structural, Functional and Smart Materials*. CRC Press, 2005.
[27] K. R. Gadelrab, F. A. Bonilla, and M. Chiesa, “Densification modeling of fused silica under nanoindentation,” *Journal of Non-Crystalline Solids*, vol. 358, no. 2, pp. 392–398, Jan. 2012.
[28] I. Jauberteau, M. Nadal, and J. L. Jauberteau, “Atomic force microscopy investigations on nanoindentation impressions of some metals: effect of piling-up on hardness measurements,” *Journal of Materials Science*, vol. 43, no. 17, pp. 5956–5961, Sep. 2008.
[29] J. M. Wheeler and J. Michler, “Elevated temperature, nano-mechanical testing in situ in the scanning electron microscope,” *Review of Scientific Instruments*, vol. 84, no. 4, p. 045103, 2013.
[30] E. Arzt, “Size effects in materials due to microstructural and dimensional constraints: a comparative review,” *Acta materialia*, vol. 46, no. 16, pp. 5611–5626, 1998.
[31] M. D. Uchic, “Sample Dimensions Influence Strength and Crystal Plasticity,” *Science*, vol. 305, no. 5686, pp. 986–989, Aug. 2004.
[32] S. S. Brenner, “Tensile Strength of Whiskers,” *Journal of Applied Physics*, vol. 27, no. 12, p. 1484, 1956.
[33] K. W. McElhaney, J. J. Vlassak, and W. D. Nix, “Determination of indenter tip geometry and indentation contact area for depth-sensing indentation experiments,” *Journal of Materials Research*, vol. 13, no. 5, pp. 1300–1306, 1998.
[34] M. F. Ashby, “The deformation of plastically non-homogeneous materials,” *Philosophical Magazine*, vol. 21, no. 170, pp. 399–424, 1970.
[35] G. Feng and W. D. Nix, “Indentation size effect in MgO,” *Scripta Materialia*, vol. 51, no. 6, pp. 599–603, Sep. 2004.
[36] J.-Y. Kim, B.-W. Lee, D. T. Read, and D. Kwon, “Influence of tip bluntness on the size-dependent nanoindentation hardness,” *Scripta Materialia*, vol. 52, no. 5, pp. 353–358, Mar. 2005.
[37] Y. Liu and A. H. W. Ngan, “Depth dependence of hardness in copper single crystals measured by nanoindentation,” *Scripta Materialia*, vol. 44, no. 2, pp. 237–241, 2001.
[38] R. K. Abu Al-Rub, “Prediction of micro and nanoindentation size effect from conical or pyramidal indentation,” *Mechanics of Materials*, vol. 39, no. 8, pp. 787–802, Aug. 2007.

[39] M. Rester, C. Motz, and R. Pippan, “Microstructural investigation of the volume beneath nanoindentations in copper,” *Acta Materialia*, vol. 55, no. 19, pp. 6427–6435, Nov. 2007.
[40] W. D. Nix, J. R. Greer, G. Feng, and E. T. Lilleodden, “Deformation at the nanometer and micrometer length scales: Effects of strain gradients and dislocation starvation,” *Thin Solid Films*, vol. 515, no. 6, pp. 3152–3157, Feb. 2007.
[41] C. A. Volkert and E. T. Lilleodden, “Size effects in the deformation of sub-micron Au columns,” *Philosophical Magazine*, vol. 86, no. 33–35, pp. 5567–5579, Nov. 2006.
[42] D. Kaufmann, *Size Effects on the Plastic Deformation of the BCC-metals Ta and Fe*. Cuvillier, 2011.
[43] S. M. Han, T. Bozorg-Grayeli, J. R. Groves, and W. D. Nix, “Size effects on strength and plasticity of vanadium nanopillars,” *Scripta Materialia*, vol. 63, no. 12, pp. 1153–1156, Dec. 2010.
[44] C. R. Weinberger and W. Cai, “Surface-controlled dislocation multiplication in metal micropillars,” *Proceedings of the National Academy of Sciences*, vol. 105, no. 38, pp. 14304–14307, 2008.
[45] O. Franke, J. C. Trenkle, and C. A. Schuh, “Temperature dependence of the indentation size effect,” *Journal of Materials Research*, vol. 25, no. 07, pp. 1225–1229, Jul. 2010.
[46] V. Maier, M.J. Cordill, and D. Kiener, “Small scale deformation of Chromium – Influence of Microstructure & Temperature,” presented at the MSE 2014, Darmstadt.
[47] S. Vadalakonda, R. Banerjee, A. Puthcode, and R. Mirshams, “Comparison of incipient plasticity in bcc and fcc metals studied using nanoindentation,” *Materials Science and Engineering: A*, vol. 426, no. 1–2, pp. 208–213, Jun. 2006.
[48] C. Shin and S. Shim, “Dislocation mechanisms of radius effect on displacement bursts during spherical nanoindentations,” *Journal of Materials Research*, vol. 27, no. 16, pp. 2161–2166, Aug. 2012.
[49] H. Bei, E. George, J. Hay, and G. Pharr, “Influence of Indenter Tip Geometry on Elastic Deformation during Nanoindentation,” *Physical Review Letters*, vol. 95, no. 4, Jul. 2005.
[50] K. L. Johnson and K. L. Johnson, *Contact Mechanics*. Cambridge University Press, 1987.
[51] T. Suzuki and T. Ohmura, “Ultra-microindentation of silicon at elevated temperatures,” *Philosophical Magazine A*, vol. 74, no. 5, pp. 1073–1084, Nov. 1996.
[52] C. A. Schuh, C. E. Packard, and A. C. Lund, “Nanoindentation and contact-mode imaging at high temperatures,” *Journal of Materials Research*, vol. 21, no. 03, pp. 725–736, Mar. 2006.
[53] J. F. Smith and S. Zheng, “High temperature nanoscale mechanical property measurements,” *Surface Engineering*, vol. 16, no. 2, pp. 143–146, 2000.
[54] J. M. Wheeler, R. A. Oliver, and T. W. Clyne, “AFM observation of diamond indenters after oxidation at elevated temperatures,” *Diamond and Related Materials*, vol. 19, no. 11, pp. 1348–1353, Nov. 2010.
[55] J. M. Wheeler and J. Michler, “Invited Article: Indenter materials for high temperature nanoindentation,” *Review of Scientific Instruments*, vol. 84, no. 10, p. 101301, 2013.
[56] A. Lupinacci, J. Kacher, A. Eilenberg, A. A. Shapiro, P. Hosemann, and A. M. Minor, “Cryogenic in situ microcompression testing of Sn,” *Acta Materialia*, vol. 78, pp. 56–64, Oct. 2014.

[57] S.-W. Lee, Y. Cheng, I. Ryu, and J. R. Greer, “Cold-temperature deformation of nano-sized tungsten and niobium as revealed by in-situ nano-mechanical experiments,” *Science China Technological Sciences*, vol. 57, no. 4, pp. 652–662, Apr. 2014.
[58] “Tungsten single crystal.” [Online]. Available: http://mateck.com/index.php?option=com_content&view=article&id=34&crys=31&Itemid=7&virtuemart_category_id=67. [Accessed: 10-Mar-2015].
[59] “Copper.” [Online]. Available: http://mateck.com/index.php?option=com_content&view=article&id=82&Itemid=7&virtuemart_category_id=17. [Accessed: 10-Mar-2015].
[60] “Chromium.” [Online]. Available: http://mateck.com/index.php?option=com_content&view=article&id=80&Itemid=7&virtuemart_category_id=15. [Accessed: 10-Mar-2015].
[61] E. Lassner and W. D. Schubert, *Tungsten: Properties, Chemistry, Technology of the Element, Alloys, and Chemical Compounds*. Springer US, 2012.
[62] D. Roundy, C. R. Krenn, M. L. Cohen, and J. W. Morris, “The ideal strength of tungsten,” *Philosophical Magazine A*, vol. 81, no. 7, pp. 1725–1747, Jul. 2001.
[63] A. J. Schwartz, M. Kumar, and B. L. Adams, *Electron Backscatter Diffraction in Materials Science*. Kluwer Academic, 2000.
[64] Y.-T. Cheng and C.-M. Cheng, “Scaling relationships in indentation of power-law creep solids using self-similar indenters,” *Philosophical Magazine Letters*, vol. 81, no. 1, pp. 9–16, 2001.
[65] W. J. Poole, M. F. Ashby, and N. A. Fleck, “Micro-hardness of annealed and work-hardened copper polycrystals,” *Scripta Materialia*, vol. 34, no. 4, pp. 559–564, 1996.
[66] “Factors Affecting Nanoindentation Test Data,” in *Introduction to Contact Mechanics*, Springer New York, 2000, pp. 61–82.
[67] S. Ogata, “Ideal Pure Shear Strength of Aluminum and Copper,” *Science*, vol. 298, no. 5594, pp. 805–807, Oct. 2002.
[68] D. Wu and T. G. Nieh, “Incipient plasticity and dislocation nucleation in body-centered cubic chromium,” *Materials Science and Engineering: A*, vol. 609, pp. 110–115, Jul. 2014.
[69] D. Wu, J. R. Morris, and T. G. Nieh, “Effect of tip radius on the incipient plasticity of chromium studied by nanoindentation,” *Scripta Materialia*, vol. 94, pp. 52–55, Jan. 2015.
[70] V. Maier, C. Schunk, M. Göken, and K. Durst, “Microstructure-dependent deformation behaviour of bcc-metals – indentation size effect and strain rate sensitivity,” *Philosophical Magazine*, vol. 95, no. 16–18, pp. 1766–1779, Jun. 2015.
[71] Shin Takeuchi, Tatsuo Hasimoto, Koji Maeda, “Plastic deformation of bcc metal single crystals at very low temperatures.” .
[72] J. N. Wang, “A new modification of the formulation of Peierls stress,” *Acta Materialia*, vol. 44, no. 4, pp. 1541 – 1546, 1996.
[73] S.-W. Lee, L. Meza, and J. R. Greer, “Cryogenic nanoindentation size effect in [0 0 1]-oriented face-centered cubic and body-centered cubic single crystals,” *Applied Physics Letters*, vol. 103, no. 10, p. 101906, 2013.
[74] W. C. Oliver and G. M. Pharr, “Measurement of hardness and elastic modulus by instrumented indentation: Advances in understanding and refinements to methodology,” *Journal of materials research*, vol. 19, no. 01, pp. 3–20, 2004.
[75] P. Sudharshan Phani, K. E. Johanns, E. P. George, and G. M. Pharr, “A stochastic model for the size dependence of spherical indentation pop-in,” *Journal of Materials Research*, vol. 28, no. 19, pp. 2728–2739, Oct. 2013.

[76] J. K. Mason, A. C. Lund, and C. A. Schuh, “Determining the activation energy and volume for the onset of plasticity during nanoindentation,” *Physical Review B*, vol. 73, no. 5, Feb. 2006.
[77] M. Laurent-Brocq, E. Béjanin, and Y. Champion, “Influence of roughness and tilt on nanoindentation measurements: A quantitative model: Influence of Roughness and Tilt,” *Scanning*, p. n/a–n/a, Apr. 2015.
[78] C. Klüber, “Orientierungsabhängigkeit und Größeneffekte bei der Nanoindentierung von Einkristallen,” *Diss. Universitätsbibliothek*, 2008.